In the format provided by the authors and unedited.

Late Middle Pleistocene Levallois stone–tool technology in southwest China

Yue Hu[1], Ben Marwick[1,2]*, Jia–Fu Zhang[3], Xue Rui[1], Ya–Mei Hou[4,5], Jian–Ping Yue[4,5], Wen–Rong Chen[6], Wei–Wen Huang[4] & Bo Li[1,7]*

[1]Centre for Archaeological Science, School of Earth and Environmental Sciences, University of Wollongong, Wollongong, New South Wales, Australia. [2]Department of Anthropology, University of Washington, Seattle, WA, USA. [3]MOE Laboratory for Earth Surface Processes, Department of Geography, College of Urban and Environmental Sciences, Peking University, Beijing, China. [4]Key Laboratory of Vertebrate Evolution and Human Origins, Institute of Vertebrate Paleontology and Paleoanthropology, Chinese Academy of Sciences, Beijing, China. [5]CAS Centre for Excellence in Life and Paleo-environment, Beijing, China. [6]Qianxi County Bureau of Cultural Relics Protection, Bijie, China. [7]ARC Centre of Excellence for Australian Biodiversity and Heritage, University of Wollongong, Wollongong, New South Wales, Australia. *e-mail: bmarwick@uw.edu; bli@uow.edu.au

SUPPLEMENTARY INFORMATION

SI section 1

Supplementary Discussion │ Geological and archaeological background

<u>Introduction to Guanyindong Cave</u>

Guanyindong Cave (26°51′26″N, 105°58′7″E, 1464 m a.s.l.) is located in the Qianxi county of Guizhou province, the eastern end of the Yungui Plateau, Southwest China (Fig. 2). This region has a typical karst landscape (Extended Data Fig. 1) with a general elevation of 1400–2000 m, and is composed of carboniferous and Permian limestones, cataclastic rocks, basalt, and coal deposits. The main ecosystem types include evergreen broad-leaved forest, coniferous and broad-leaved mixed forest, and montane elfin forest. With a subtropical humid climate (humid in summer and dry in spring), this region is controlled by the East Asian summer monsoon and the cold fronts of the winter monsoon and the southwest warm-wet air masses [1]. The mean annual temperature is about 14 °C, with the highest monthly mean temperature (20–21 °C) in summer and the lowest (4–5 °C) in winter. Mean annual precipitation in this region is ~1400 mm.

Guanyindong Cave is a limestone cave developed during the Late Tertiary or beginning of the Quaternary [2], and is one of the highest and most developed karst caves in this region. The cave, extending from east to west, was developed from a fracture that was mainly formed by an east-west strike, joint with several south-north branches (Extended Data Fig. 2a). The main entrance, which is also the main excavation area, is located at the west end of the cave. The cave, about 90 m long and 2–4 m wide, has a narrow roof that gradually broadens down to the floor. The distance from floor to roof is about 2–8 m high. The cave floor is about 15 m above the bottom of the depression.

The sedimentary deposits slope down from the entrance to the inside of the cave (Extended Data Fig. 2b), and there is a general trend of decreasing grain size of sediments from outside to inside [2], indicating that the source of the deposit came mainly from the outside. Stalactites and stalagmites are well developed inside the cave, and some of them are connected, forming stalagnates. Thick flowstone plates were developed surrounding the stalagnates at various areas in the cave, these plates cover the majority of sediment in the cave, but the thickness of the plates varies.

The Guanyindong Cave site was first discovered in 1964 by a field team organised by the Institute of Vertebrate Paleontology and Paleoanthropology and the Provincial Museum of Guizhou. Four excavation seasons were conducted in 1964, 1965, 1972 and 1973, respectively. Several trenches (Profiles 1, 2a, 2b and 3) were opened within the cave (Extended Data Fig. 2a) in the 1960s, which yielded about a hundred stone artefacts. The main excavation was conducted in the 1970s at the west cave entrance (Extended Data Fig. 2a), where most of the fauna fossils and stone artefacts were found [2].

<u>Stratigraphy and fossil assemblage</u>

The deposits at the site are mainly sandy/silty clays with limestone and breccia fragment inclusions. According to the excavation report by the original excavators [2,3], the stratigraphy of the sediments at the main entrance was divided into 9 layers (Layers 1–9) (Extended Data Fig. 2a) and 3 groups: Group A (Layer 2), Group B (including Layers 3–8) and Group C (Layer 9) [2]. While Layer 1 and Group B extend from the outside to the inside of the cave, Layer 2 (Group A) was found in front of the cave entrance only (Extended Data Fig. 2b). Most sediments from Layer 1, Groups A and B in the main excavation area had been removed during the previous excavations. In 2015, we visited the cave and found a ~3m residual profile, named S1, which is located at the south-wall near the cave entrance (Extended Data Figs 2b and 3a).The Layer 1, Groups B and

C were still visible at S1 (Extended Data Figs. 3b, c). In 2018, we re-visited the site and found another residual profile, S2, at the south wall, about 14 m away from the cave entrance (Extended Data Figs 2b and 4), where the Layer 1 and Layer 2 are exposed. The stratigraphic features of the two profiles are consistent with those described by the excavators [3]. The features of each layer are described in Supplementary Table 1.

The fossils from Group A are mostly fragments [2], indicating that the material of Group A was probably reworked before deposition. Only a few species were identified, including *Rhinoceros sinensis Owen*, *Stegodon sp.*, *Hystrix sp.* and *Bovinae*. In contrast to Group A, the fossils from Group B were much better preserved, and abundant species can be identified, including 23 families [*Eulota (Cathaica) sp.*, Testudinidae indet., *Macaca sp.*, *Hystrix cf. subcristata Swinhoe*, *Rhizomys cf. sinensis Gray*, *Vulpes cf. vulgaris* L., *Ursus thibetanus kokeni* M. et G., *Ailuropoda melanoleuca fovealis* M. et G., *Mustelidae indet.*, *Crocuta ultima Matsumoto*, *Panthera cf. tigris* L., *Gomphotheriidae indet.*, *Stegodon cf. orientalis* Owen, *Stegodon guizhouensis* Li et Wen sp. nov., *Equus sp.*, *Megatapirus augustus* M. et *G.*, *Rhinoceros sinensis* Owen, *Sus cf. scrofa L.*, *Muntiacus sp.*, *Cervus (cf. Pseudaxis) sp.*, *Rusa sp.,* Bovinae, and *Capricornis sumatraensis* Bechstein] and 13 species (*Gastropoda*, *Chelonia*, *Primates*, *Rodentia*, *Carnivora*, *Proboscidea*, *Perissodactyla* and *Artiodactyla*). Most of these species belong to the Middle Pleistocene *Ailuropoda-Stegodon* fauna group, which is commonly found at cave sites in South China.

Previous chronological studies

There were a few attempts to date the Guanyindong site since the 1980s. The first dating work was conducted by Yuan et al. [4] using U-series dating on fossil teeth recovered directly from the stratigraphic units of the site. In their study, a total of 6 fossil teeth were dated, including one from Layer 2 (Group A), one from Layer 4, three from Layer 5 and one from Layer 8 (Supplementary Table 1). Given the complexity and difficulty of quantifying uranium migration into and out of skeletal tissues, the U-series results on bones and teeth should be regarded as minimum age estimates [5]. The U-series age of the fossil tooth from Layer 2 is 55 ± 3 ka, hence, providing a minimum estimate for the age of Group A. The other U-series ages obtained for the fossil teeth from Group B range from ~75 to ~120 ka, placing a minimum age of ~120 ka for the Layer 4 and those below.

The second atempt was conducted by Shen and Jin [6], based on U-series dating on carbonate and fossil teeth. In their study, samples were taken from three locations (named Profiles 1, 2a and 3 by Pei et al. [3]) inside the cave (Extended Data Fig. 2c). Profile 1 is located at the cave entrance. Profiles 2a and 3 are two of the earliest test pits excavated by Pei et al. [3] in the 1960s. They are located further inside the cave, where very few artefacts (~100 stone artefacts) were found and many of them were collected from the surface. Since the artefacts excavated inside the cave are not analysed in our study, we focus our discussion on Shen and Jin's dating results for the samples from the cave entrance only. A total of 8 samples were collected from the cave entrance (see Extended Data Fig. 2a for their plane locations). The first two samples (QGC-19-1 and QGC-19-2) were taken from the bottom tip of a hanging stalactite, yielding ages of 58 ± 3 and 42 ± 2 ka, respectively. The authors claimed that this stalactite "has sign of residual red clay on the bottom surface", indicating that this stalactite was in contact with the red-clay deposits from Layer 2 and, hence, should provide a maximum age estimate for Layer 2. However, this age is younger than the U-series age (~55 ka) of the fossil tooth extracted in-situ from Layer 2 reported by Yuan et al. [4]; the latter should be viewed as a minimum age of Layer 2. Furthermore, according to the stratigraphic description by Li and Wen [2] (see Extended Data Fig. 2b), the deposits of Layer 2 terminated outside the cave, so the 'red-clay attachement' on the stalactite

should not be linked to the Layer 2, and, therefore, its age should not be used to constrain the age of Layer 2. Our OSL age of ~80 ka for Layer 2 also confirms that their age estimates for Layer 2 are underestimated.

The third sample (QGC-4) is a piece of broken stalactite sitting on top of "some residual deposits" at the north wall, which yielded an age of > 350 ka, and it should not be linked to any stratigraphic unit of the site. The fourth sample (QGC-12) is "a piece of flowstone sitting on top of some residual deposits attached to the north wall of the cave". This sample yielded an age of 52 ± 2 ka. According to Shen and Jin, this sample has the same elevation as Layer 4, and they regarded this age as an estimate of the age of Layer 4. However, this age is significant younger than the minimum age (~119 ka) obtained from the fossil teeth directly taken from Layer 4 reported by Yuan et al. [4], suggesting that the correlation of the sample and Layer 4 simply based on their elevation is unreliable.

The fifth sample (QGC-21) is a piece of carbonate 'curtain' taken on the north wall but a few tens of centimeters below QGC-12. This sample yielded an age of 147 ± 14 ka. Given the failed correlation of the overlying sample QGC-12 mentioned above, the stratigraphic location of QGC-21 remains unclear. The sixth sample (QGB-4) is a rhinoceros tooth recovered from Layer 6 in the residual sediment profile at the south wall (where our OSL samples were taken). The U-series age of this sample is 73 ± 3 ka, and should be viewed as a minimum age for this layer. The seventh sample (QGC-7) is 'a small piece of stalagmite sitting on top of the flowstone from Layer 6' of the residual profile at the south wall. The age of this sample is 185 ± 15 ka, providing a reliable constraint of the age for this layer. The last sample (QGC-23) is an in-situ stalagmite from the bottom of the profile at the north wall, which yielded an age of 260 ± 30 ka. This age should provide a reliable constraint of the maximum age for Layer 8 or Group B.

In conclusion, previous U-series dating on fossil teeth and carbonate have provided controversial results, mainly because many of the analysed carbonate samples lack firm stratigraphic control. As a result, only those samples with a reliable stratigraphic control can provide useful constraints on the chronological framework of this site (Supplementary Table 1). For this reason, all of the U-series ages of fossil teeth extracted directly from sediments should be viewed as minimum ages for the associated layers, and only one stalagmite sample (QGC-7) taken directly from Layer 6 from the residual profile at the south wall yielded reliable age estimate for this layer (~180 ka).

SI section 2

Supplementary Discussion │ Guanyindong Cave lithic analysis

Previous analyses of Guanyindong Cave lithics

The classification of Levallois products remains a subjective matter, on which analysts often disagree [7-9]. As one of the most important Palaeolithic sites in Southern China, Guanyindong is no exception to this, with previous studies coming to differing conclusions about the presence of Levallois in the Guanyindong Cave assemblage.

One of the earliest English-language sources [10] describes casts of five artefacts and identifies one as a transverse concave scraper made on a pseudo-Levallois point. Anticipating additional Levallois products, Freeman concludes that he 'would venture to guess that the collection will prove to have some proto-Levallois or true Levallois flakes when it is finally studied' (p. 101). Li et al. [11] came to a different conclusion after detailed examination of 1108 stone artefacts housed in the IVPP collections. They employ the chaîne opératoire concept to conduct a 'technological reading' of the assemblage. They identified three categories of cores representing three technological systems. Neither of these 'involve intentional preparation' (p. 3869) so they conclude that the Guanyindong Cave artefacts are 'quite distinct from the concept of Levallois' and reflect 'different modes of cognition' (p. 3870). A third report mentioning Guanyindong stone artefacts summarises the assemblage and notes that 'a few Levallois-like flakes were identified' [12].

Of the three previous English-language reports on the Guanyindong Cave stone artefacts, two claim to have observed traces of Levallois in the assemblage, and one argues that it is absent. We interpret the artefacts differently than past researchers and we have made 3D models for anyone else to examine and interpret (see Supplementary Data). In our view, the analysis of Li et al., which concluded that Levallois concepts are absent from Guanyindong, is problematic because of their relying on chaîne opératoire-related methods that contribute to the irreproducibility of their results. The clarity and objectivity of chaîne opératoire methods have been widely questioned by stone artefact analysts. For example, Bar-Yosef and Van Peer argued that chaîne opératoire is '*overformalized and provides but an illusion of reading the minds of prehistoric knapper*'[13]. Similarly, Monnier and Missel [14] have noted that use of chaîne opératoire concept is '*highly subjective; being based upon the analyst's experience and intuition*" (p. 3). A well-known example of this problem can be found in the analysis of the assemblage from Biache Saint-Vaast level IIA. Boëda [15] identified unidirectional and bidirectional recurrent Levallois core reduction, but Dibble [16] found that the core reduction strategy changed from unidirectional to bidirectional as cores were more extensively reduced. This example highlights the difficulty of using the chaîne opératoire concept to obtain a result that can be reproduced by another analyst.

In their chaîne opératoire analysis, Li et al. describe three cores from Guanyindong Cave in detail (P4114, P4122, P15948). We concur with their assessment of P4114 and P4122 that these cores are not Levallois. Contrary to Li et al, however, we identify P15948 as Levallois (see Fig. 3a, Extended Data Fig. 5a and the 3D structure in Supplementary Data), and will discuss this piece in detail as an example of how our approach differs from Li et al. We disagree with Li et al. on details of the analysis of this piece: Li et al. claimed that 1) each flaking sequence is unrelated; 2) there is only one flaking sequence; 3) all the flake scars come from the same direction, 4) convexity is obtained by the flake ventral surface; and 5) the platform is not prepared. They, however, offer no explanation for one critical assumption, why they found each flaking sequence to be unrelated. On the contrary, we found each sequence to be hierarchically related. First, through faceting along the edge, the striking platform size and shape was adjusted to allow removal of flakes parallel to the plane of intersection of the upper and lower surfaces. Then, convexities were shaped and maintained

with removals based on the previously prepared striking platform. Finally, the Levallois products were split off by using a centripetal recurrent method along the fracture plane that is parallel or sub-parallel to the plane of the intersection. We consider each of these flaking sequences to be related because one sequence could not start before the other was completed. In our view there are three flaking sequences, not one, as claimed by Li et al.. In addition, rather than originating from the same direction, these scars run from multiple directions by using the Levallois recurrent centripetal method. There are two flake scars for which they did not explain the sequence ascription

Their fourth claim, that the blank of the core is a flake, is not convincing because this core is a slab or nodule with part of the cortex left on the lower surface. The most distant ends of the piece have a similar thickness of about 20–30mm. It is not like a typical Guanyindong flake which is thick at the proximal end and thin at the distal end. There are many cores that are made from flakes in Guanyindong and we describe these with the term "truncated faceting". From these cores, we can see that the scars are either too small or too scarce to be classified as Levallois, and most of them are on the edge without extending across the whole ventral surface. Even if the ventral surface was flaked, we cannot say that it was not prepared. For example, at Orgnac 3 in France, slabs are a common component of the Levallois assemblage, and half of Levallois cores take advantage of the natural convexity of a flake's ventral surface to maintain the distal and literal convexities[17,18].

Finally, we observed signs of preparation on the platform of this piece, which is not a cortical surface as reported by Li et al.. Our analysis found Levallois attributes on P15948, which presents all stages of reduction and manufacture of a Levallois core. The upper surface is covered with several scars come from different directions forming a centripetal scar pattern. Before flaking on the debitage surface, the core had been knapped along the edge to prepare the striking platform. The fractures of the predetermined flakes are parallel to the plane of the flake release surface and the striking platform surface.

Our detailed description of P15948, above, is typical of how our analysis of the Guanyindong assemblage differs from Li's. In Li's Ph.D. thesis [19] she describes 18 cores. Besides P15948, there are two more artefacts that we identified as Levallois cores (P5262 and P16311), but Li did not. For P5262, Li's conclusion is based on the assumption that the core was knapped from a naturally convex surface. But we did not find a natural convex surface, and instead observed preparation scars on its lateral and distal convexity, creating this geometry. Furthermore we found a prepared platform, contrary to Li's observation of a cortical platform. For P16311, which has the least clear scar pattern of the three pieces noted here, Li identified a joint face, but in our view there are scars resulting from upper and lower surface structures typical of Levallois pieces. The key issue for each of their pieces remains the same: we did not make assumptions about the blank's geometry, but observed it directly. We report a summary of our analysis in the following sections.

Whole assemblage characteristics: cores, flakes & retouch

We analysed 2273 artifacts in the whole assemblage which consists of 267 cores, 1195 flake pieces, 42 retouched pebbles & chunks and 769 chunks & debris (see examples shown in Extended Data Figs 5 and 6 and Supplementary Figs 21–24). The R code used to produce the results presented here is available online at http://doi.org/10.17605/OSF.IO/ERNTJ.

Chert is the dominant raw material for the assemblage (~80%). The 1195 flake pieces include a large number of retouched flakes and retouched flake breaks (n=1008), complete flakes (n=182) and a small quantity of flake fragments (n=5). While all stages of reduction and manufacture are represented, final stages are most abundant. The average maximum length of the flakes pieces is 55.5 mm, the average thickness is 16.3 mm.

Plain platform is the major type of flake platforms. The average number of scars on the dorsal side of complete flakes is three. Flakes with three dorsal scars are the largest proportion and more than 80% of flakes have four scars or less. Most of the cortex is limited, ranging from 0 to 10%. It suggests that before hominins brought knapping products into the cave they had knapped the blank outside of the cave, and, therefore, the flakes were on the later stages of knapping, with less cortex.

In total, we found 267 cores in the lithic assemblage. The average max dimension is 74.8 mm and with an average mass of 165 g. This dimension is slightly larger than the flakes. The flaking technique of Guanyindong Cave is free-hand percussion with hard hammer. The raw material of cores is dominated by chert (85%) followed by limestone (14%). There are various geometries of cores, including irregular (80%), conic (9.6%), column (6.8%) and small amounts of wedged and circle. Most cores (~80%) produced 1–4 flake scars before being discarded. Cores that have more than eight scars are rare (n = 4). The average scar length is 33 mm. Most cores are covered with zero (46.5%) or 5–20% cortex (31.5%). The majority of platform type is plain (52%), which suggests that using former scars as platform to continue flaking is the main strategy of knapping.

Five discoid cores were identified in the assemblage (see examples from Supplementary Figs 21.3, 21.4, 22.3 and 22.4). Morphologically, some of these discoid cores resemble several features with Levallois cores, but they are rejected based on the criteria of Levallois technology, mostly because either the direction of flaking is secant to the line of the plane of the upper and lower surfaces or the two surface are exchangeable. In the Guanyindong Cave assemblage, toolmakers usually selected a flat surface from the blank and then knapped around the edge forming geometries varying from conic to irregular. The average maximum dimension of discoid cores is ~64 mm. The average number of flakes obtained from a discoid core is four. Three of them have a surface covered with cortex and the platforms are mainly plain.

A total of 1050 retouched pieces were found in the assemblage (see examples from Supplementary Fig. 24), accounting for 46% of entire lithic assemblage. The average max dimension of retouched pieces is about 56 mm. Side scrapers and denticulates dominate the sub-division of retouched pieces (74%), followed by notches (9%) and borers (7%). Over 50 % (n=525) of the retouched pieces have more than one retouched edge. The shapes of 1683 retouched edges include convex, concave, straight, denticulate, end, notch, and borer. Among them, straight edge constitutes the largest proportion of the retouched edge (n=523) followed by convex (n=348) and concave (n=250).

Assemblage characteristics: prepared elements, cores and flakes

In addition to the Levallois assemblage, cores and flakes with prepared platforms, blade cores and truncated-faceted pieces are also found in the assemblage. Eighteen cores are found with prepared platforms. This type of core features facetted scars on the striking platform in order to preparing a proper angle before knapping. Shapes of these cores are mainly irregular (67%) and conic (22%). Most of them (~56%) have only one platform. The average max dimension is 79.6 mm.

There are 43 flakes with faceted platforms, 72% of which were retouched to make tools. The majority of platform shapes are quadrangle (364%) and triangle (20.5%). The average platform width and thickness is 35.2 × 11.4 mm. The average max dimension of these flakes is 62.3 mm. Only a few flakes show traces of dorsal cortex (20%) and most of them have one or more previous flake scars remaining on the dorsal surface. A small amount of blade cores were also found (see examples from Supplementary Figs 21–23). Compared with blade cores from the European Upper Palaeolithic [20], these blade cores present distinctive features. The

geometries of these cores vary from flat circle to cylinder, and are not as regular as those found in typical Upper Palaeolithic assemblages, where blade cores usually present prismatic shapes. Some of their platforms are facetted and only a few blades were obtained from each core.

Core preparation is also present on 60 truncated-faceted pieces [21-24]. These pieces usually started from a flake that was then knapped on the ventral side, ending up as cores with the flake scars on ventral side, indicating the production of invasive flakes from platforms along the dorsal edge (Supplementary Figs 21–23). Other than on cores themselves, attributes indicating core preparation are also found on flakes (see examples from Figs 3t–3z and Extended Data Figs 6–7). Furthermore, evidence for maintaining core convexities is observed from 26 débordants (Fig. 3l and Extended Data Fig. 6), blanks that remove a large part of a core's lateral edge and are typically considered to be byproducts of core maintenance [25].

Patterns in artefact reduction

To understand the technological sequences that produced the artefacts at Guanyindong Cave we investigated how flake attributes vary across different sized pieces. The distribution of flake mass is strongly right-skewed with a long tail, typical of many flaked stone artefact assemblages (Extended Data Fig. 8). The unimodal quality of this distribution does not indicate any obvious size classes suitable to use as analytical categories to compare flake attributes in different reduction stages. To divide the flakes in the assemblage into analytical categories we used a dynamic programming algorithm for optimal one-dimensional k-means clustering[26]. This method selects optimal number of clusters of flake sizes based on the Gaussian mixture model using the Bayesian information criterion (BIC). After limiting cluster membership to 30 or more artefacts, we found five clusters of size classes in the Guanyindong Cave flakes that we can use to investigate changes in flaking behaviours relative to size.

Raw materials are uniformly distributed across each size class (Extended Data Fig. 9). Cortex location shifts markedly from the left, right and distal areas of the dorsal surface for larger flakes (size class 5), to be found mostly on the platform and right side of the dorsal surface of smaller flakes (size classes 1, 2 and 3). This indicates that most small flakes result from advanced stages of the reduction process. The high proportion of flakes with cortex on the right indicates a repeated sequence of flake removals moving left to right across the face of a core. Platform shape shows a trend of an increasing proportion of rhombus platforms as flake size decreases. The "gull-wing" [27] platform (also called "platform beveling" [28]) is increasingly represented in the smaller size classes. This shape of platform resulted from the detachment of a flake directly behind the location of a previously detached flake, and has been frequently found in Levallois points [29], as well as Nubian Complex [30] and tula adze blanks [27]. This pattern in the Guanyindong assemblage indicates a high degree of precision when producing the smaller flakes.

Platform types are highly diverse throughout the reduction sequence. Missing platforms are more common on the smallest flakes. Faceting is only evident on mid- and small-sized flakes (size classes 1, 2, and 3), consistent with a Levallois strategy of preparing cores by flaking across their platforms, resulting in flakes with facetted platforms. The low proportions of faceting on large flakes indicate that this was not a generic technique applied at all reduction stages, but only preferentially applied to certain-sized flakes produced via Levallois processes. We can see further support for this in the distribution of flake types, with Levallois flakes also appearing only in the mid- and small-sized flakes. This indicates a well-controlled reduction strategy where the production of Levallois flakes was constrained to a specific size range. Kombewa flakes are most abundant in the largest size class. This type of flake is distinctive due to having two opposed bulbs of percussion because it is detached at the intersection of the platform and ventral surface of a larger flake. The

8

rarity of Kombewa flake in the smaller sized flakes reflects the high levels of inertia and precision required to detach a flake from a larger flake

The distribution of retouch types shows complex variation across the reduction sequence. Only subtle changes in proportions are evident across the size classes. The three smaller size classes have the greatest diversity and most even distribution of retouch types. This indicates how retouch types present in the larger size class, such as scrapers, notched pieces, borers and denticulate pieces, are transformed into new types, such as tanged pieces, points, and end-scrapers, as reduction of a piece proceeds further and the mass of the pieced is reduced by reduction.

Extended Data Fig. 8 shows that as for larger flakes sizes, the oriented thickness and flake thickness (at 25%, 50% and 75% of the length axis) all increase only very slightly, relative to increases in mass, length, oriented width, platform width and platform thickness, which increase substantially. For the most part, flake thickness is thus less than expected for larger flakes. This indicates that the thickness of larger flakes was controlled by the knappers at the start of the reduction sequence, consistent with a deliberate strategy to produce flakes with desirable features in tools, such as capacity for retouch and reduction of torque. The percentage of dorsal cortex varies little, from a median of 10% to 0%, but with a higher range in the larger flakes. This indicates even the largest flakes often do not have much cortex on their dorsal surface, so some pre-processing of the artefacts must have happened before they arrived at Guanyindong Cave. The median and range in the number of flake scars is nearly constant across size classes.

Artefact taphonomy

Among the flake pieces in the assemblage, 63% (n = 748) are broken, among which most of them are retouched. Two processes are likely responsible for this high percentage: manufacturing failures during the knapping activity, and energetic taphonomic processes that have damages the artefacts after discard. The generally homogenous nature of the stone indicates that failures during knapping should be expected at a low frequency, assuming a competent knapper. The sedimentary feature of the deposits (characterised by well stratified and sorted silt and sand layers) inside the cave indicates a low-energy depositional process. Thus, many of the breakages may be attributed to post-depositional processes such as ground surface breakage due to trampling. We found two artefacts that can be refitted (Supplementary Fig. 22.12). Many of the artifacts show considerable edge rounding/chipping, indicating some form of taphonomic influence. For example, trampling and post-depositional processes may have damaged artefact edges in ways that resemble light retouch, which may partly explain the high percentage (46%) of retouched pieces in the whole assemblage. With just two artefacts showing signs of heat treatment, we conclude that artefact damage due to excess heating occurred at a negligible rate at Guanyindong Cave. The surface texture of the artefacts is generally fresh, indicating limited weathering from exposure to pedogenic processes. This is probably a result of the cool, dry environment within the rockshelter.

Chronological change in the lithic assemblage

The artefacts that we analyzed were collected during excavations in 1964–1973, when it was not typical to record artefact provenance at high spatial resolutions. Thus, only a small amount of the stone artefact assemblage contains provenance information that allows us to determine what period of time is represented. A total of 204 pieces of the studied stone artefacts have clear stratigraphic information, with 117 pieces from the lower layer (Group B, 170–160 ka) and 87 from the upper layer (Group A, ~90–80 ka). Only five Levallois

pieces included information about which layer they were recovered from (3 from the upper layer, 2 from the lower layers). This small number of artefacts with chronological context limits the robustness of any claims we can make about change over time at Guanyindong Cave. Nevertheless, the patterns that are evident provide support to our main claim for Levallois technology appearing here at 170–80 ka.

Extended Data Fig. 10 shows that flakes are slightly larger in the upper layer, and more variable in the thickness dimensions. Limestone is more frequently utilized as a raw material in the upper layer, as well as a small amount of sandstone, which does not appear in the lower level assemblage. This minor increase in raw material breadth in the upper layer may relate to a decrease in the availability of chert on the landscape, perhaps due to increased vegetation cover during MIS 5 that may result in changes in forager mobility strategies. Most of the technological attributes show little difference between the upper and lower layers, indicating that the technological strategies were similar across the two periods. Notable differences include platform shape, where we see higher proportions of rhombus and gull-wing platforms in the lower layer. We also see a much higher proportion of facetted platforms in the lower layer. The high frequency of platform faceting in the lower layer is notable because faceting is a key step in the preparation of striking platforms on Levallois cores. While this attribute by itself is not sufficient to identify a piece as Levallois, the high frequency of it in the lower layer is consistent with this period (170–80 ka) as a time when the cave's occupants were producing Levallois technology.

SI section 3

Supplementary Table 1 | Description of stratigraphic layers, number of stone artefacts, together with ages (±1σ error) obtained from samples that have reliable stratigraphic age control and associated dating methods. Note that the U-series ages of fossils should be regarded as minimum age estimates.

Layer	Thickness (cm)	Sedimentary features	Number of stone artefacts	Age (ka) / Method / Reference
1	~15–70	Archaeologically sterile and consists of black silty clay	0	• 40–70 (OSL on 3 sediment samples) (this study)
Group A				
2	~40–240	Reddish-yellow silty clay, containing abundant rock debris and plenty of stone artefacts and fragments of mammal fossils. This layer sits unconformably on top of Group B (Extended Data Fig. 2b).	879	• 57 ± 3 (U-series on a rhinoceros tooth) [4] • 87 ± 3 (weighted mean of 4 OSL samples) (this study)
Group B				
3	~50–100	A loose layer with brown-yellow and grey-yellow silty clay, containing fragments of limestone and breccias. According to the excavation report, this layer yielded only a small number of stone artefacts and fossils.	20	
4	~40–50	Brown-yellow and red-yellow silty clay with some fragments of limestone breccias. The top of this layer is capped by a flowstone layer (3–5 cm in thickness). Many stone artefacts and fossils were found from this layer.	68	• 119 ± 10 (U-series on a unknown fossil tooth) [4] • 163 ± 12 (weighted mean of 2 OSL samples) (this study)
5	~20	Grey silty clay with abundant limestone fragments, which yielded plenty of stone artefacts and fossils.	801	• 84 ± 5 (U-series on a *Bovinae* tooth) [4] • 76 ± 4 (U-series on a unknown fossil tooth) [4] • 104 ± 6 (U-series on a rhinoceros tooth) [4] • 163 ± 12 (OSL on sediment) (this study)
6	~10	Similar to Layer 4 but with the absence of large limestone fragments. This layer yielded more stone artefacts and fossils than Layer 4.	236	• 73 ± 3 (U-series on a rhinoceros tooth) [6] • 181 ± 16 (U-series on stalagmite) [6] • 175 ± 32 (OSL on sediment) (this study)
7	~15	A grey-yellow silty clay layer containing stone artefacts and fossils with abundant small limestone fragments.	139	• 167 ± 12 (OSL on sediment) (this study)
8	~10	Yellow silty clay, containing limestone and breccias fragments. Stone artefacts and fossils were found from this layer too.	20	• 115 ± 7 (U-series on a *Cervidae* tooth) [4] • 169 ± 14 (OSL on sediment) (this study)
Group C				
9	> 10 cm	Archaeologically sterile and consists of layers of sand, gravels and breccias.	0	• 260 ± 30 (U-series on stalagmite) [6]

Supplementary Table 2 | Summary of the sites shown in Fig. 1, together with their corresponding ages and dating methods used. For some sites, precise numerical ages are not available because absolute dating methods were not applied and their ages were only roughly estimated by stratigraphic correlation, so only MIS stages were provided for these sites. All uncertainties are expressed at 1σ.

ID	Site	Country	Age (ka)	MIS stage	Dating method	Reference
1	Guanyindong	China		6–4	OSL/U-series	This study
	AFRICA					
2	Bundu farm	South Africa	190–340	9	ESR	[31]
3	Kathu Pan	South Africa	291 ± 45	9	OSL/ESR/U-seires	[32]
4	Kibish formation	Ethiopia	~195	7	Ar/Ar	[33,34]
5	ETH72-8B & Kulkuletti (Gademotta formation)	Ethiopia	~280	8	Ar/Ar	[33]
6	Florisbed	South Africa	268 ± 26	8	ESR, OSL	[35]
7	Sterkfontein cave	South Africa	252 ± 42	8	ESR/stratigraphy	[31]
8	Gademotta	Ethiopia	180–280	8	Ar/Ar	[31,36]
9	Kulkuletti	Ethiopia	~280 ± 8	8	Ar/Ar	[31,36]
10	Border cave	South Africa	217–238	7	ESR	[31]
11	Kapthurin formation	Kenya	200–250	7	Tephra	[33,37]
12	Kharga oasis & site REF-4	Egypt	220 ± 20	7	U-series	[38]
13	Sai island	Sudan	152–223	7	OSL	[39]
	EUROPE					
14	Achenheim	France	258 ± 23	9	stratigraphy	[40]
15	Ambrona	Spain	336 ± 36	9	ESR / U-series	[41]
16	Aridos 1	Spain		9	stratigraphy	[42]
17	Atapuerca	Spain	345 ± 26	9	ESR / U-series	[43]
18	Dall'Olio Cave	Italy		9	stratigraphy	[44]
19	Domeny	Spain	> 317 ± 49	9	Ar/Ar, stratigraphy	[45]
20	Gentelles base	France		9	stratigraphy	[44]
21	La Micoque	France	288–350	9	ESR/U-series	[46]
22	Cagny Lépinette	France		9	stratigraphy	[47]
23	Orgnac 3	France	> 303	9	Ar/Ar, U-Th	[48]
24	Petit bost	France	325 ± 30	9	TL	[49]
25	Puig den Roca	Spain	< 317 ± 49	9	Ar/Ar, stratigraphy	[45]
26	Purfleet	UK	~ 324	9	TL, stratigraphy	[50]
27	Solent River	UK		9	stratigraphy	[51]
28	Torralba	Spain	> 243 ± 18	9	U-series, stratigraphy	[52]
29	Torre in Pietra	Italy		9	stratigraphy	[53]
30	Argoeuves	France		8	stratigraphy	[54]
31	Baume Bonne	France		8	stratigraphy	[55]
32	Kesselt -Op de Schanz	Belgium		8	stratigraphy	[48]
33	Les Bossés	France	274 ± 12	8	TL	[56]
34	Markkleeberg	Germany		8	stratigraphy	[57]
35	Mesvin	Belgium	283 ± 30	8	U-Th	[58]
36	Raspide 2	France		8	stratigraphy	[59]
37	Rheindahlen	Germany		8	stratigraphy	[60]
38	Abri Vaufrey	France	208 ± 8	7	U-series	[61]
39	Bapaume les (Pas-De-Calais)	France	~195	7	IRSL	[62]
40	Bečov I	Czech Republic		7	stratigraphy	[63]
41	Biache-Saint-Vaast	France	230 ± 18	7	ESR/U-series/TL	[64]
42	Biśnik Cave	Poland	230 ± 51	7	TL	[65]
43	Bonneval	France	240	7	TT-OSL	[66]
44	Campsas	France		7	stratigraphy	[67]
45	Cantalouette	Ukraine	223 ± 20	7	TL/stratigraphy	[68]

ID	Site	Country	Age (ka)	MIS stage	Dating method	Reference
46	Dzierżysław	Poland		7	stratigraphy	[69]
47	Galeria Pesada	Portugal	241 ± 22	7	ESR/U-series	[70]
48	Gran Rois	France		7	stratigraphy	[62]
49	Hundisburg	Germany		7	stratigraphy	[71]
50	Korolevo	Ukraine	220 ± 35	7	OSL	[72]
51	La Cotte de St.Brelade	UK	238 ± 35	7	TL	[73]
52	Le Pucheuil	France		7	stratigraphy	[74]
53	Le Rissori(MSJ)	Belgium		7	stratigraphy	[75]
54	Maastricht Belvédère	Netherlands	258 ± 19	7	TL/ESR	[76]
55	Nové Mesto nad Váhom	Slovakia		7	stratigraphy	[69]
56	Raciborz Studienna 2	Poland		7	stratigraphy	[69]
57	Salouël	France	> 200 ± 57	7	ESR/U-series	[77]
58	San Bernardino	Italy	184 ± 6	7	ESR	[78]
59	Thames valley	UK		7	stratigraphy	[79]
60	Therdonne	France	178 ± 11	7	TL/stratigraphy	[80]
61	Weimar-Ehringsdorf	Germany	230	7	U-Th	[81]
62	Susiluola Cave	Finland	> 100	5	OSL, TL, stratigraphy	[82]
	ASIA					
63	Attirampakkam	India	385 ± 64	9	OSL	[83]
64	Nor Geghi	Armenia	335–325	9	Ar/Ar, stratigraphy	[71]
65	Denisova Cave	Russia	220–280	8	TL	[84]
66	Hayonim	Israel	~ 220	7	TL/ESR	[85]
67	Misliya Cave	Israel	177–194	6	ESR/U-series	[86]
68	Hummal	Syria	150–220	7	TL	[87]
69	Jebel Qattar JQ-1	Saudi Arabia	211 ± 16	7	OSL	[88]
70	Karain cave	Turkey	250–200	7	TL/ESR	[89]
71	Misliya cave	Israel	166–212	7	TL	[90]
72	Tabun(Mount Carmel)	Israel	256 ± 26	7	TL/ESR	[91]
73	Mikhailovskoe	Russia		9–7	stratigraphy	[92]
74	Obi-Rakhmat Grotto	Uzbekistan	55–73	6	ESR, OSL	[93]
75	Ust-Karakol 1	Russia	133 ± 33	6–5	TL	[94,95]
76	Aybut al Auwal	Oman	106	5	OSL	[96]
77	Bogdanovka	Russia		5	stratigraphy	[97]
78	Garchi I	Russia	~115	5	OSL	[98,99]
79	Jwalapuram (JPW 3a)	India	74–77	5	OSL	[100]
80	Katoati	India	50–100 or older	5	OSL	[101]
81	Khotyk	Russia		5	TL	[82]
82	Myshtulagty Lagat	Russia	70–250	5–7	Ar/Ar, stratigraphy	[102]
83	Ust'-Izhul	Russia	~125	5	IRSL	[103]
84	Kara-Bom	Russia	~62	4	ESR	[95,104]
85	Shergarh Tri-Junction	India	60–43	4	OSL	[105,106]
86	Jinsitai	China	41–28	3	C-14	[107]
87	Okladnikov Cave	Russia	45–33	3	U-series, C-14	[104,108]
88	Shuidonggou Locality I	China	38–34	3	C-14	[109-111]
89	Tsagaan Agui	Mongolia	<70–90	5–3	TL	[112,113]

13

Supplementary Table 3 | Number of single grains or aliquots measured, rejected and accepted for each sample, together with the reasons for their rejection.

Sample	Grain size (μm)	Number of measured	T_n below 3σ above BG [a]	RSE of T_n > 20% [a]	Recuperation > 5%	Poor DRC [a]	D_e by extrapolation	No L_n/T_n intersection	Rejected	Accepted D_e values [b]	Proportion of saturated [c]
GYD-OSL1	90–150	800	224	221	3	199	22	32	701	99 (12%)	35%
	180–212	1000	619	272	1	85	1	8	986	14 (1%)	39%
GYD-OSL2	90–125	800	148	210	2	203	42	15	620	180 (23%)	24%
	180–212	4200	2820	979	11	291	2	12	4115	85 (2%)	14%
GYD-OSL3	90–125	600	138	134	0	187	19	24	502	98 (16%)	30%
	180–212	800	505	210	1	59	1	4	780	20 (3%)	20%
GYD-OSL4	90–180	1400	680	346	5	225	7	29	1292	108 (8%)	25%
GYD-OSL5	90–180	1500	631	451	4	274	19	29	1408	92 (6%)	34%
	180–212	1000	662	217	1	94	1	6	981	19 (2%)	27%
GYD-OSL6	90–180	1000	441	284	3	190	9	18	945	55 (6%)	33%
	180–212	800	558	170	1	56	0	0	785	15 (2%)	0%
GYD-OSL7	90–125	600	308	147	6	54	0	15	530	70 (12%)	18%
GYD-OSL8	90–125	500	147	116	16	92	0	25	396	104 (21%)	19%
GYD-OSL9	90–125	500	149	114	12	93	0	39	407	93 (19%)	30%
GYD-OSL10	90–125	1000	390	317	43	147	16	24	937	63 (6%)	39%
GYD-OSL11	90–125	600	248	222	15	77	6	9	577	23 (4%)	39%
GYD-OSL12	90–125	1000	412	269	28	148	14	24	895	105 (11%)	27%
GYD-OSL13	90–125	500	204	159	8	69	9	14	463	37 (7%)	38%

[a] BG, RSE and DRC represent background, relative standard error and dose response curve, respectively.

[b] The proportion of grains with acceptable D_e values is shown in the parentheses and was calculated as a ratio to the total number of measured grains.

[c] The proportion of saturated grains was calculated as the number of grains with D_e obtained by extrapolation and those without L_n/T_n intersection divided by the total number of grains that passed the first four criteria (columns 4–7).

Supplementary Table 4 | Summary of number of grains with saturated natural signal and D_e estimation results based on LS-normalised L_n/T_n for individual DRC groups and different grain sizes of each sample. All uncertainties are expressed at 1σ.

Sample	Grain size (µm)	DRC Group	Number of accepted DRCs	Number of saturated grains	Over-dispersion (%)	Age model [a]	D_e (Gy) [b]	Final D_e (Gy) [d]
S1								
GYD-OSL1	90–150	1	49	25	92 ± 9	FMM-2 (84%)	saturated	
		2	57	23	75 ± 7	FMM-2 (95%)	238 ± 31	208 ± 14
		3	47	7	114 ± 12	FMM-3 (72%)	199 ± 15	
	180–212	1	9	3	144 ± 36	nMAD (78%)	saturated	211 ± 27
		2	14	2	70 ± 14	nMAD (71%)	211 ± 27	
GYD-OSL2	90–125	1	21	11	40 ± 6	nMAD (90%)	saturated	
		2	66	26	69 ± 6	FMM-3 (89%)	204 ± 30	224 ± 18
		3	68	12	74 ± 7	FMM-4 (72%)	198 ± 20	
		4	82	9	99 ± 8	FMM-4 (67%)	260 ± 20	
	180–212	1	4	1	-	- [c]	-	
		2	32	10	59 ± 8	FMM-2 (91%)	157 ± 29	198 ± 16
		3	27	3	98 ± 14	FMM-3 (59%)	203 ± 33	
		4	36	2	139 ± 17	FMM-4 (53%)	211 ± 22	
GYD-OSL3	90–125	1	67	23	76 ± 7	FMM-4 (73%)	saturated	
		2	51	17	80 ± 8	FMM-2 (78%)	226 ± 15	237 ± 13
		3	23	4	50 ± 8	FMM-3 (65%)	258 ± 24	
	180–212	1	5	2	11 ± 5	CAM (100%)	saturated	206 ± 42
		2	20	3	207 ± 34	FMM-3 (55%)	206 ± 42	
GYD-OSL4	90–180	1	53	20	202 ± 22	FMM-4 (55%)	saturated	
		2	94	23	204 ± 16	FMM-4 (41%)	292 ± 50	292 ± 50
		3	2	0	135 ± 69	-	- [c]	
GYD-OSL5	90–180	1	16	9	14 ± 3	nMAD (75%)	saturated	
		2	72	28	29 ± 3	nMAD (88%)	232 ± 30	224 ± 12
		3	52	12	67 ± 7	FMM-3 (79%)	222 ± 13	
	180–212	1	7	5	3 ± 9	CAM (100%)	saturated	
		2	12	3	71 ± 16	FMM-2 (75%)	217 ± 36	217 ± 36
		3	7	0	126 ± 37	- [c]	-	
GYD-OSL6	90–180	1	42	20	74 ± 8	FMM-2 (93%)	saturated	168 ± 12
		2	40	7	81 ± 9	FMM-3 (80%)	168 ± 12	
	180–212	1	7	1	125 ± 39	- [c]	-	
		2	8	0	98 ± 26	- [c]	-	
GYD-OSL7	90-125	1	22	14	12 ± 3	nMAD (82%)	saturated	
		2	34	2	37 ± 5	nMAD (91%)	85 ± 5	81 ± 4
		3	29	0	59 ± 8	FMM-3 (72%)	74 ± 6	

Sample	Grain size (µm)	DRC Group	Number of accepted DRCs	Number of saturated grains	Over-dispersion (%)	Age model [a]	D_e (Gy) [b]	Final D_e (Gy) [d]
GYD-OSL8	90-125	1	31	22	12 ± 2	nMAD (87%)	saturated	99 ± 4
		2	36	3	24 ± 3	nMAD (78%)	109 ± 4	
		3	40	0	16 ± 2	nMAD (83%)	93 ± 3	
		4	22	0	36 ± 6	nMAD (82%)	93 ± 6	
GYD-OSL9	90-125	1	22	18	21 ± 4	nMAD (86%)	saturated	115 ± 5
		2	46	18	14 ± 2	nMAD (85%)	129 ± 39	
		3	39	4	23 ± 3	nMAD (87%)	122 ± 7	
		4	25	0	35 ± 5	nMAD (88%)	106 ± 7	
S2								
GYD-OSL10	90-125	1	25	18	9 ± 2	nMAD (96%)	saturated	272 ± 11
		2	34	13	27 ± 4	nMAD (88%)	248 ± 37	
		3	30	7	28 ± 4	nMAD (83%)	258 ± 29	
		4	14	2	36 ± 8	nMAD (79%)	276 ± 12	
GYD-OSL11	90-125	1	11	8	19 ± 5	CAM (100%)	saturated	201 ± 24
		2	16	3	45 ± 8	FMM-2 (75%)	181 ± 41	
		3	11	4	104 ± 23	nMAD (82%)	209 ± 29	
GYD-OSL12	90-125	1	32	16	16 ± 3	nMAD (88%)	saturated	202 ± 17
		2	41	12	27 ± 3	FMM-2 (37%)	saturated	
		3	50	8	29 ± 3	FMM-2 (66%)	192 ± 20	
		4	20	2	55 ± 9	FMM-3 (60%)	220 ± 30	
GYD-OSL13	90-125	1	14	7	11 ± 3	nMAD (93%)	saturated	214 ± 16
		2	24	14	20 ± 4	nMAD (71%)	290 ± 132	
		3	20	3	15 ± 3	nMAD (85%)	212 ± 16	
		4	2	0	9 ± 6	- [c]	-	

[a] The percentage of grains used for D_e estimation is shown in parentheses.

[b] The D_e shown as 'saturated' means that the weighted mean of LS-normalised L_n/T_n is statistically consistent with the saturation level of the corresponding SGC.

[c] The number of accepted grains are insufficient for reliable statistical analysis, i.e., there is less than 5 grains that are statistically identified from the same D_e component.

[d] The final D_e were obtained based on the weighted mean of the finite D_e values obtained from each of the groups.

Supplementary Table 5 | Dose rate data, equivalent doses (D$_e$) and OSL ages for sediment samples from the Guanyindong site.

Sample	Layer / Group	Depth (cm)	Grain size (µm)	Water content (%) [a]	Gamma dose rate (Gy/ka)	Beta dose rate (Gy/ka)	Cosmic dose rate (Gy/ka) [b]	Total dose rate (Gy/a)	D$_e$ (Gy) [c]	Age (ka) [c]	Final age (ka) [c,d,e]
S1											
GYD-OSL7	1	10	90–125	20 ± 5 (17)	0.97 ± 0.03	0.99 ± 0.05	0.031	2.00 ± 0.05	81 ± 4	41 ± 2	41 ± 2
GYD-OSL8	1	50	90–125	20 ± 5 (14)	0.89 ± 0.02	1.18 ± 0.09	0.030	2.10 ± 0.09	99 ± 4	47 ± 3	47 ± 3
GYD-OSL9	1	75	90–125	20 ± 5 (11)	0.60 ± 0.02	1.04 ± 0.08	0.027	1.66 ± 0.08	115 ± 5	69 ± 5	69 ± 5
GYD-OSL1	4/B	210	90–150	30 ± 8 (20)	0.59 ± 0.05	0.69 ± 0.04	0.024	1.30 ± 0.07	208 ± 14	160 ± 14	161 ± 12
			180–212		0.59 ± 0.05	0.66 ± 0.04	0.024	1.28 ± 0.07	211 ± 27	165 ± 23	
GYD-OSL2	4/B	235	90–125	30 ± 8 (21)	0.39 ± 0.04	0.89 ± 0.06	0.023	1.30 ± 0.07	224 ± 18	173 ± 17	165 ± 12
			180–212		0.39 ± 0.04	0.84 ± 0.06	0.023	1.25 ± 0.07	198 ± 16	158 ± 15	
GYD-OSL3	5/B	245	90–125	30 ± 8 (24)	0.44 ± 0.04	0.97 ± 0.06	0.023	1.43 ± 0.08	237 ± 13	165 ± 13	163 ± 12
			180–212		0.44 ± 0.04	0.92 ± 0.06	0.023	1.38 ± 0.08	206 ± 42	149 ± 32	
GYD-OSL4	6/B	260	90–180	30 ± 8 (23)	0.49 ± 0.04	1.16 ± 0.08	0.022	1.67 ± 0.09	292 ± 50	175 ± 31	175 ± 32
GYD-OSL5	7/B	270	90–180	30 ± 8 (20)	0.42 ± 0.04	0.89 ± 0.06	0.022	1.34 ± 0.07	224 ± 12	167 ± 12	167 ± 12
			180–212		0.42 ± 0.04	0.87 ± 0.06	0.022	1.31 ± 0.07	217 ± 36	166 ± 29	
GYD-OSL6	8/B	290	90–180	30 ± 8 (20)	0.42 ± 0.04	0.54 ± 0.03	0.022	0.99 ± 0.05	168 ± 12	170 ± 14	170 ± 14
S2											
GYD-OSL10	2/A	80	90–125	30 ± 8 (28)	1.25 ± 0.03	1.59 ± 0.10	0.132	2.96 ± 0.11	272 ± 11	92 ± 5	92 ± 5
GYD-OSL11	2/A	95	90–125	30 ± 8 (32)	1.04 ± 0.02	1.54 ± 0.11	0.126	2.70 ± 0.11	201 ± 24	75 ± 9	75 ± 9
GYD-OSL12	2/A	120	90–125	30 ± 8 (31)	0.87 ± 0.02	1.28 ± 0.09	0.120	2.28 ± 0.09	202 ± 17	89 ± 8	89 ± 8
GYD-OSL13	2/A	190	90–125	30 ± 8 (30)	1.11 ± 0.02	1.36 ± 0.10	0.108	2.57 ± 0.10	214 ± 16	83 ± 7	83 ± 7

[a] Values used for dose rate and age calculations, with measured (field) water contents shown in parentheses.
[b] Values after correction for the zenith angular distribution of cosmic rays.
[c] The uncertainties provided after the ± symbol represent the uncertainty at 1σ.
[d] A systematic error of 2% was added (in quadrature) to the propagated random errors in the final ages to allow for any bias associated with the calibration of the laboratory beta sources.
[e] For samples with two grain sizes measured, their final ages were obtained based on the weighted mean of the ages obtained from each of the two grain sizes.

SI section 4
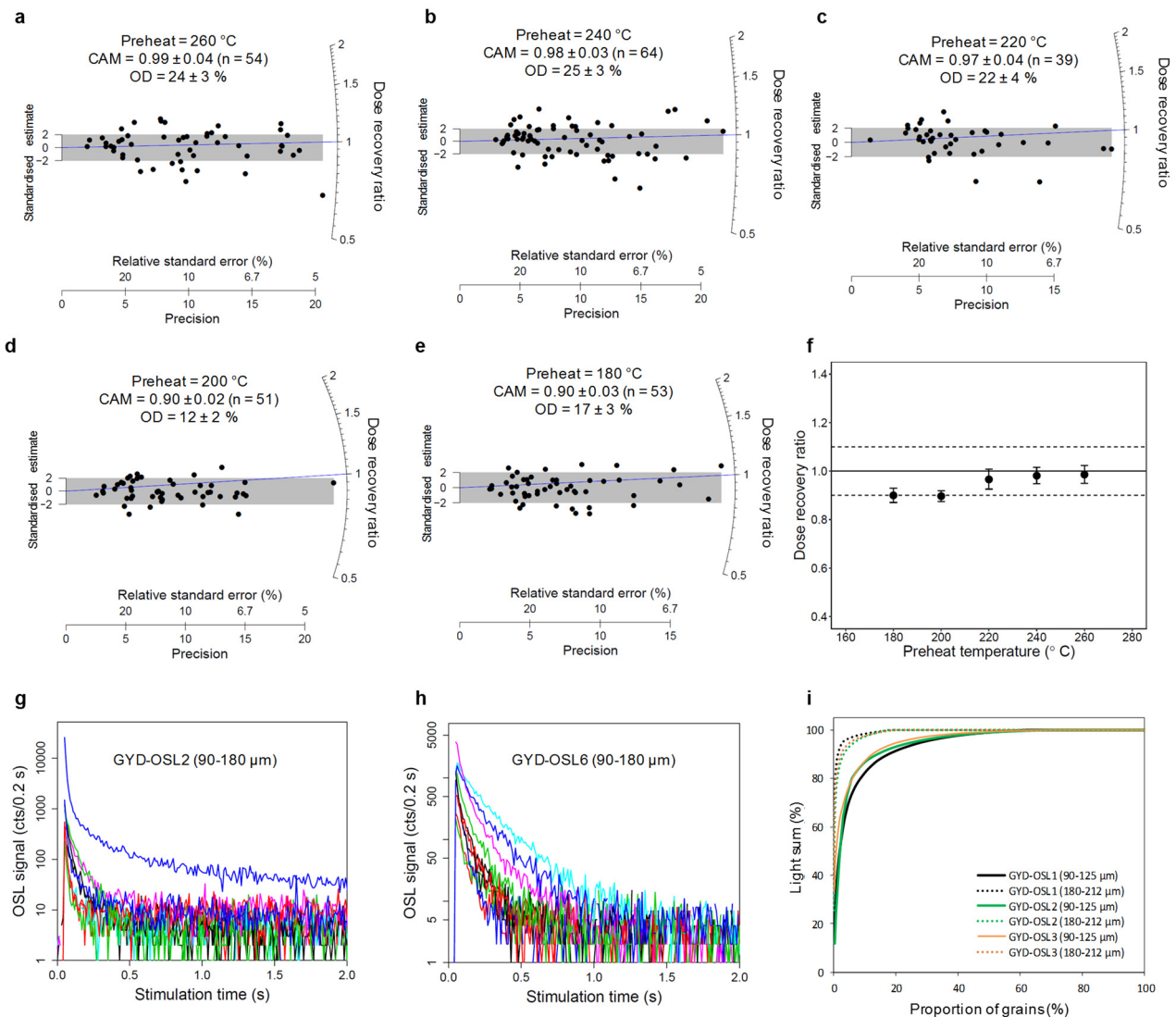
Supplementary Figure 1 | Dose recovery results and luminescence characteristics. a–e, Radial plots showing the distributions of dose recovery ratios for individual grains from GYD-OSL2 using different preheat temperatures (from 260 to 180 °C, respectively) and the corresponding CAM and OD values. **f,** The weighted mean dose recovery ratios obtained from panels a–e plotted against preheat temperature. The vertical bars represent 1σ standard error. **g–h,** Selected typical natural OSL decay curves of 10 grains from each of samples GYD-OSL2 and -OSL6, respectively. **i,** Distribution of OSL signal intensities for individual quartz grains for different grain sizes from samples GYD-OSL1, -OSL2 and -OSL3. Data are plotted as the proportion of the total light sum that originates from the specified percentage of grains.
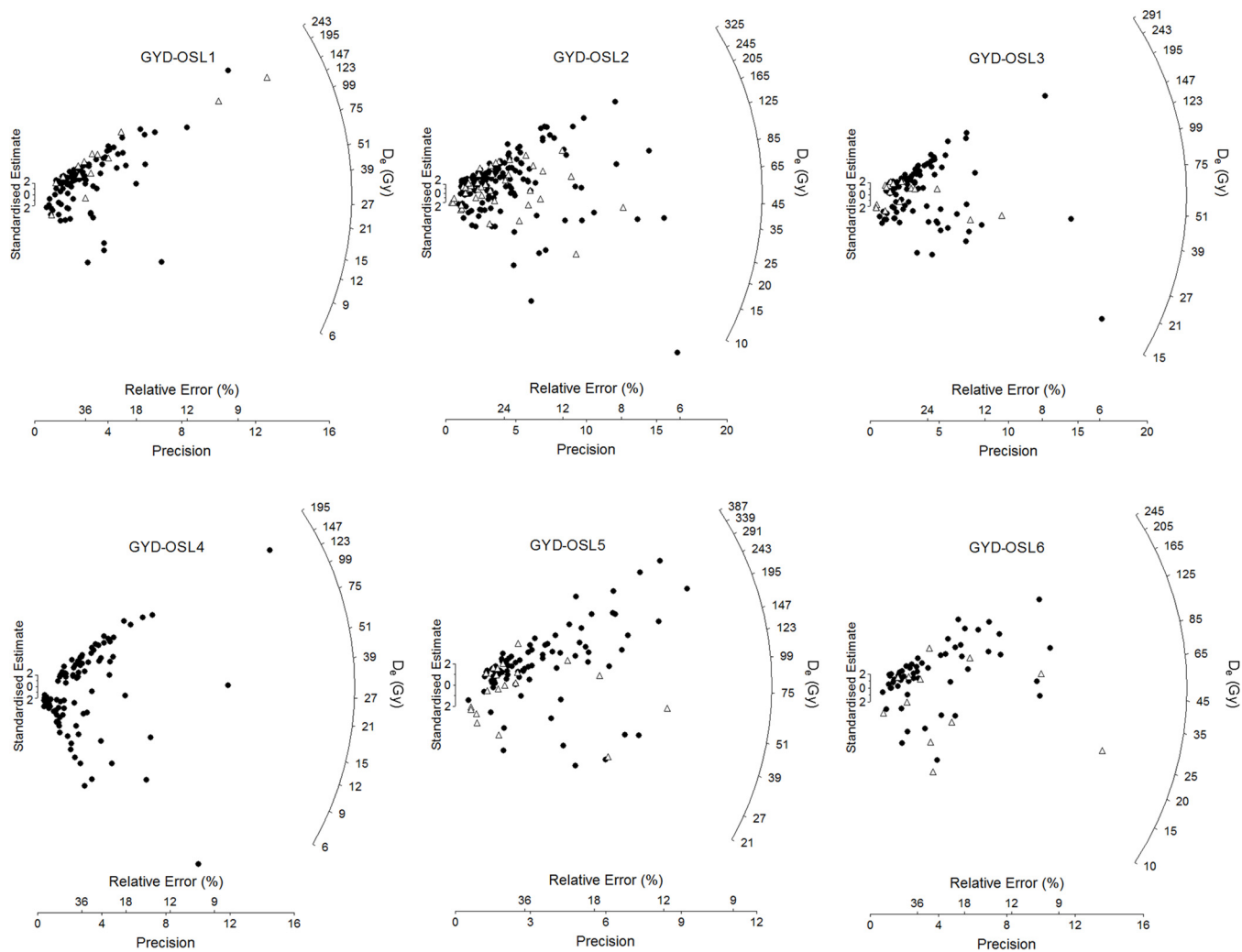
Supplementary Figure 2 | Single-grain SAR D$_e$ results for all the OSL samples. For those samples (GYD-OSL1, 2, 3, 5 and 6) where two grain sizes were measured, the filled circles are the results from the 180–212 μm size fraction and the open triangles are those from the smaller grain size (< 180 μm). See the next page for more figures.

19
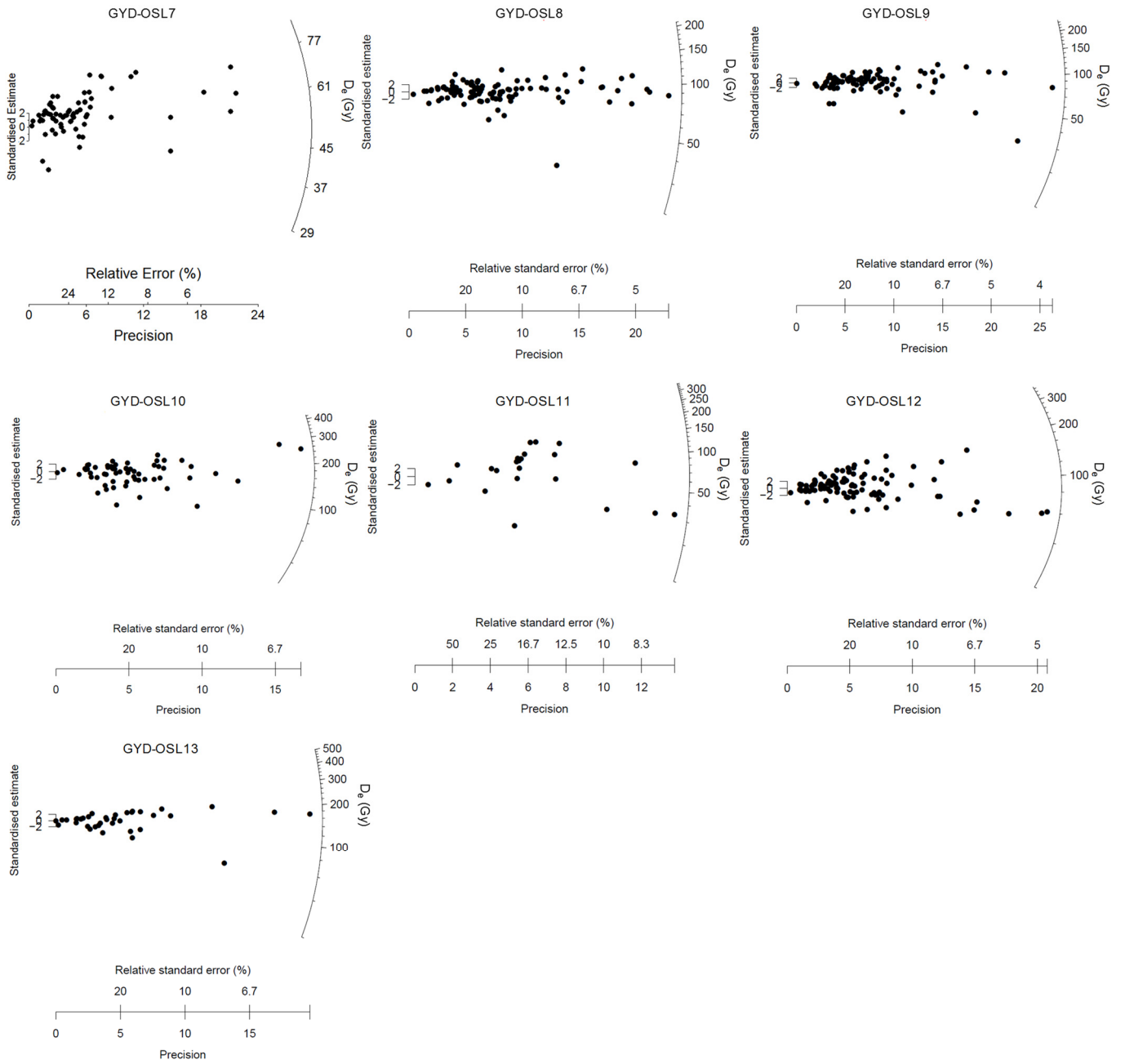
Supplementary Figure 2 continued | see the previous page for caption.
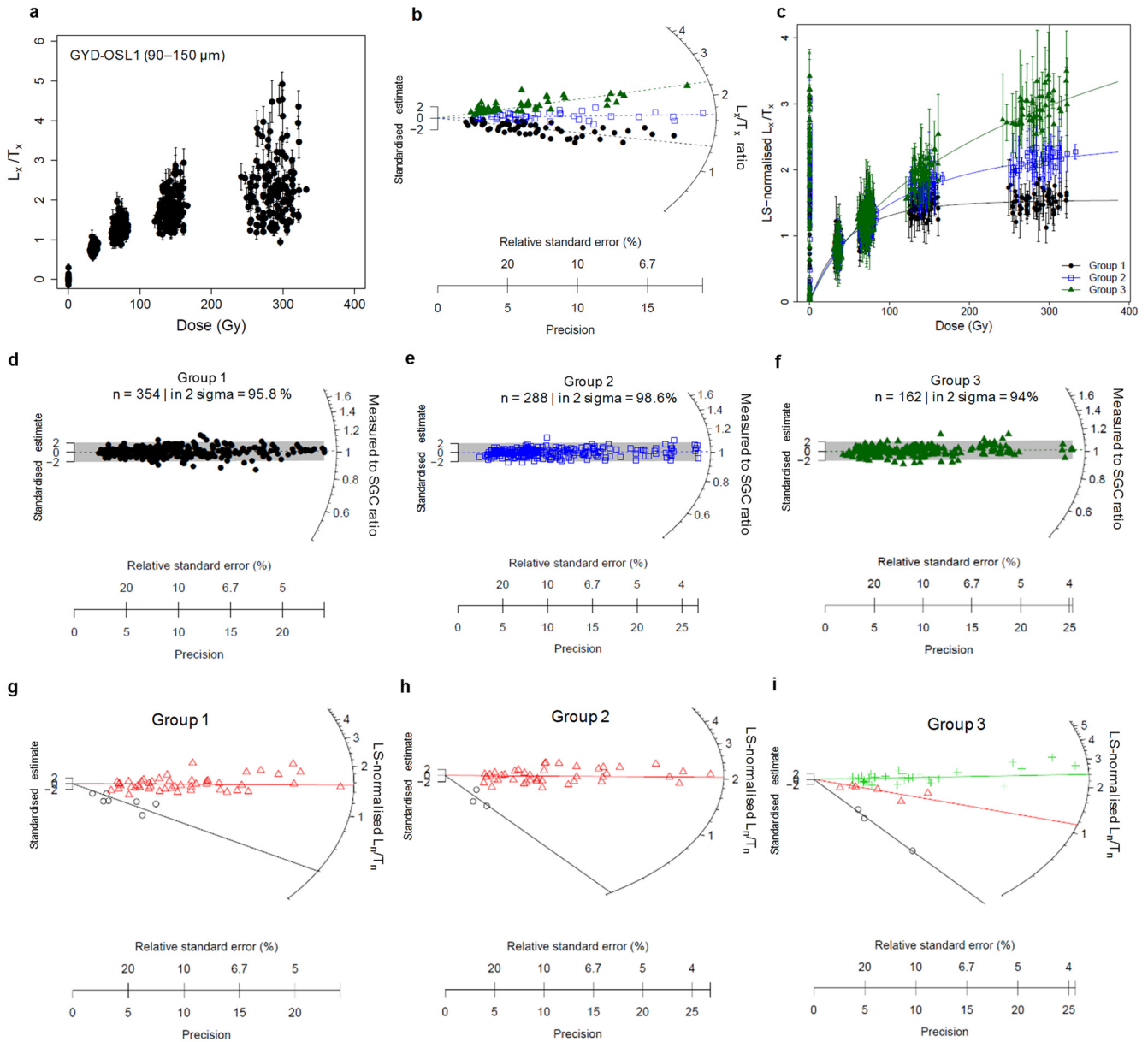
Supplementary Figure 3 | Single-grain DRCs and SGC results for the 90–150 μm grains of sample GYD-OSL1. a, Comparisons of all the DRCs that pass the rejection criteria. **b,** Radial plot showing the distribution of the ratios of L_x/T_x values between two regenerative doses of ~280 and ~70 Gy for all the accepted grains. Different symbols represent different groups of grains identified using FMM. **c,** Comparison of the LS-normalised L_n/T_n and L_x/T_x for different groups. The data set for each group were fitted using a GOK function (full lines) and then normalised to unity at 50 Gy. **d–f,** Radial plots showing the ratios between the LS-normalised L_x/T_x and the expected values from the best-fit SGCs shown in panel c; the shaded band captures 2σ range from unity. The total number of grains (n) and percentage falling inside the 2σ band are shown for each group. **g–i,** Radial plots showing the LS-normalised natural signals (L_n/T_n); different age groups were identified using FMM and distinguished using different symbols. The full lines represent the central values of individual groups obtained using FMM. All the figures and data analysis were based on the building functions in R packages "Luminescence" [114] and "numOSL" [115]. All the error bars in panels a and c represent 1σ standard error.
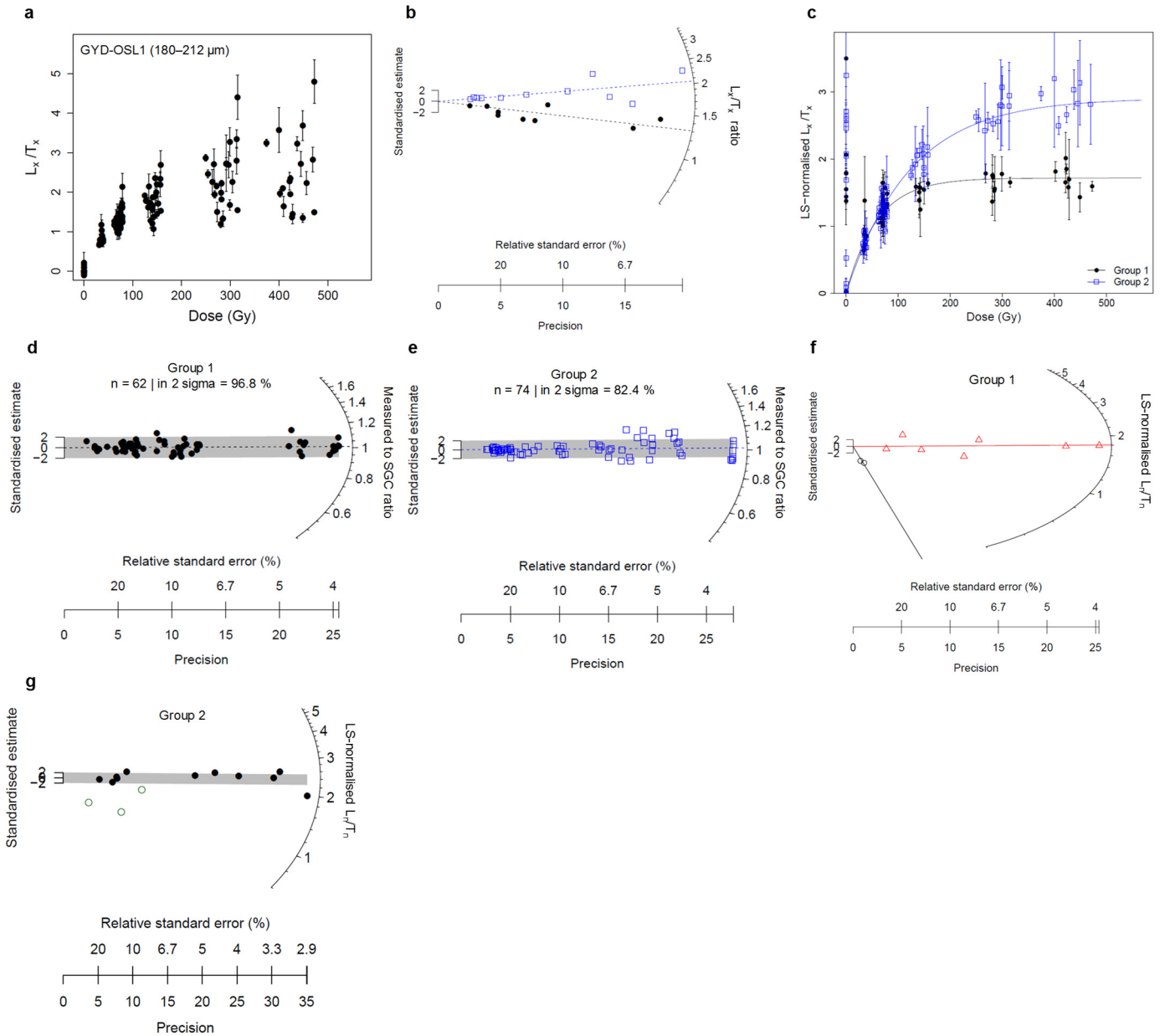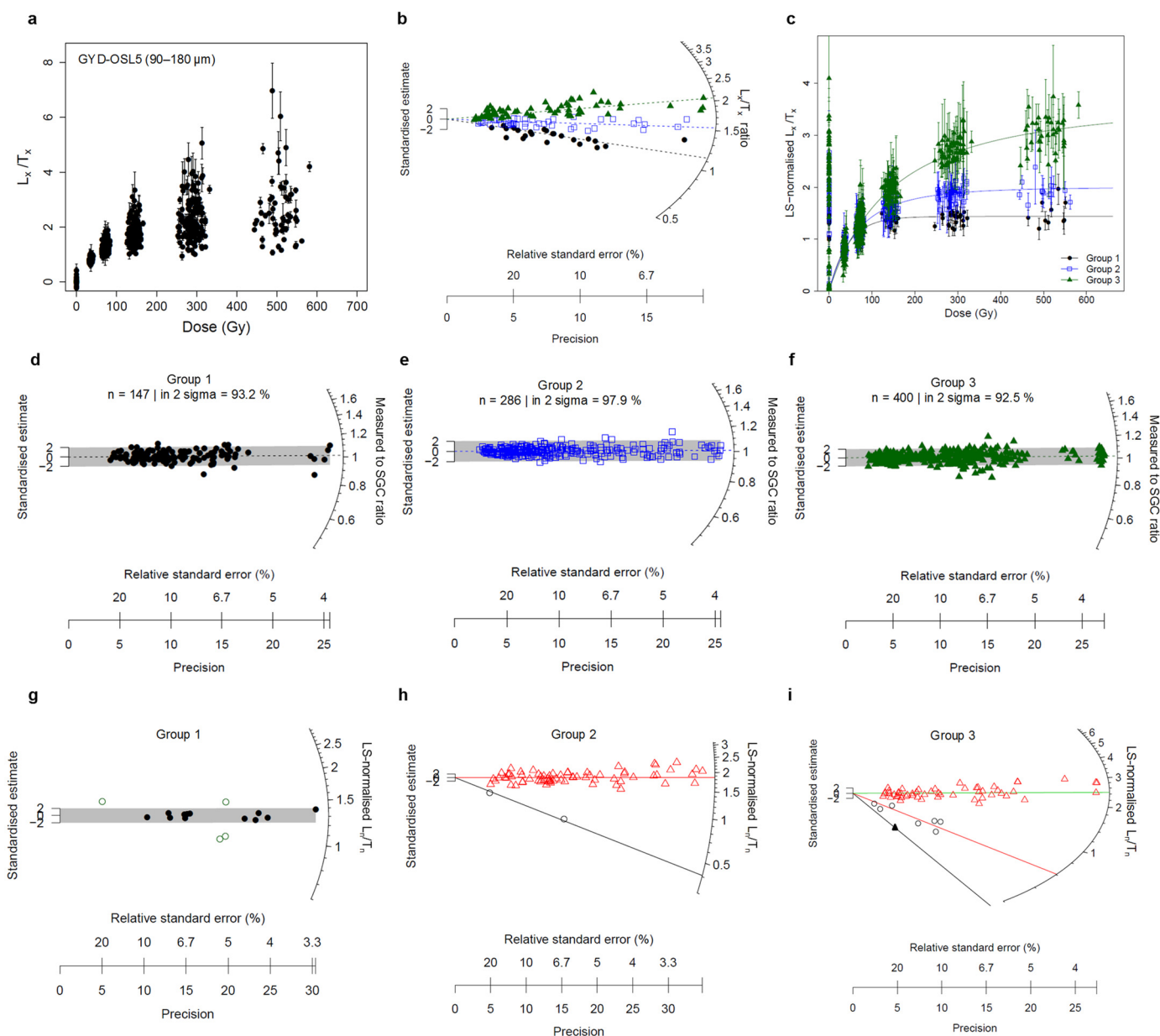
Supplementary Figure 4 | Single-grain measurement results for the 180–212 μm fraction of sample GYD-OSL1. a–c, Results similar to those described in Supplementary Figs 3a–c. **d–e,** Results similar to those described in Supplementary Figs 3d–f. **f,** Re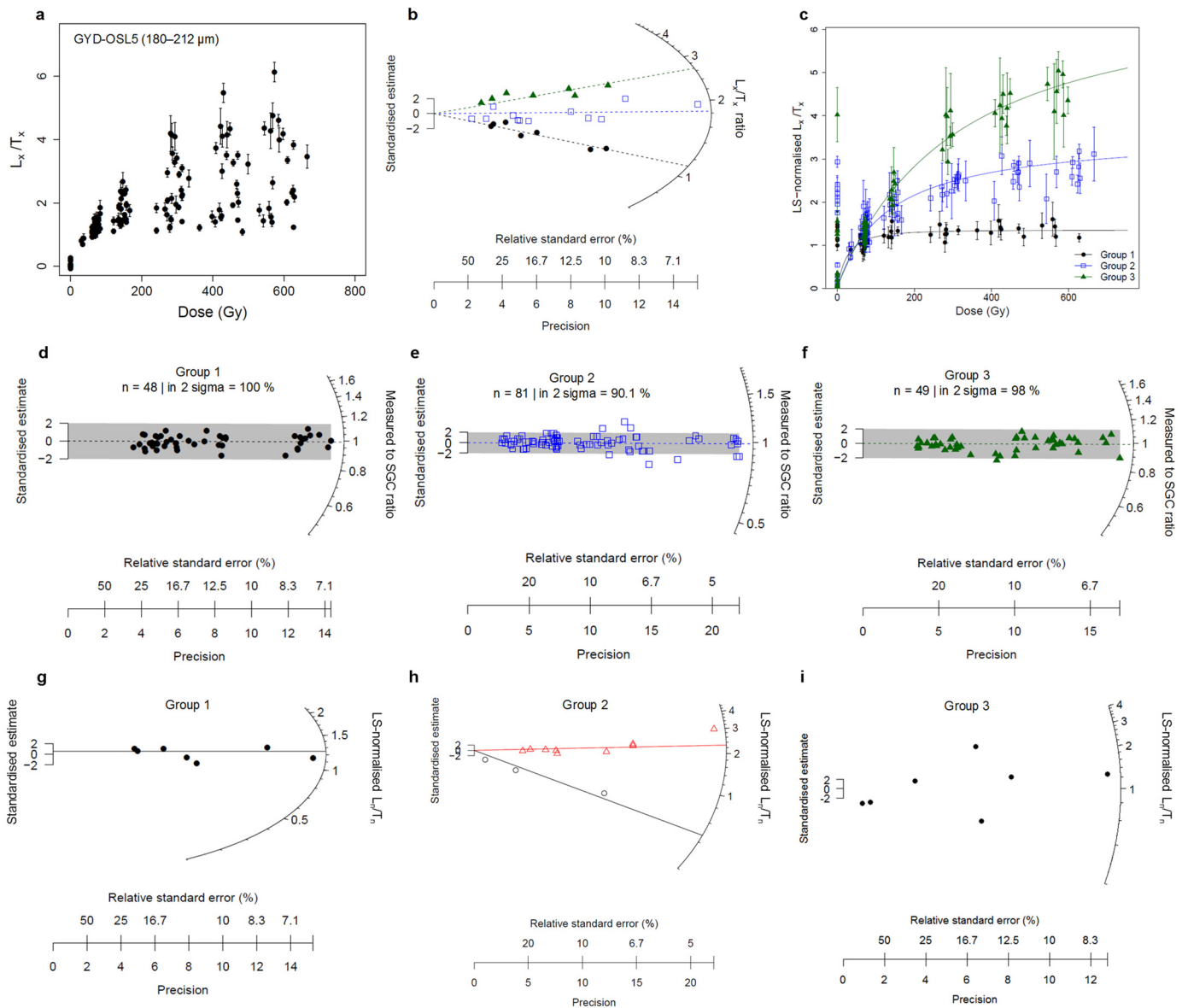s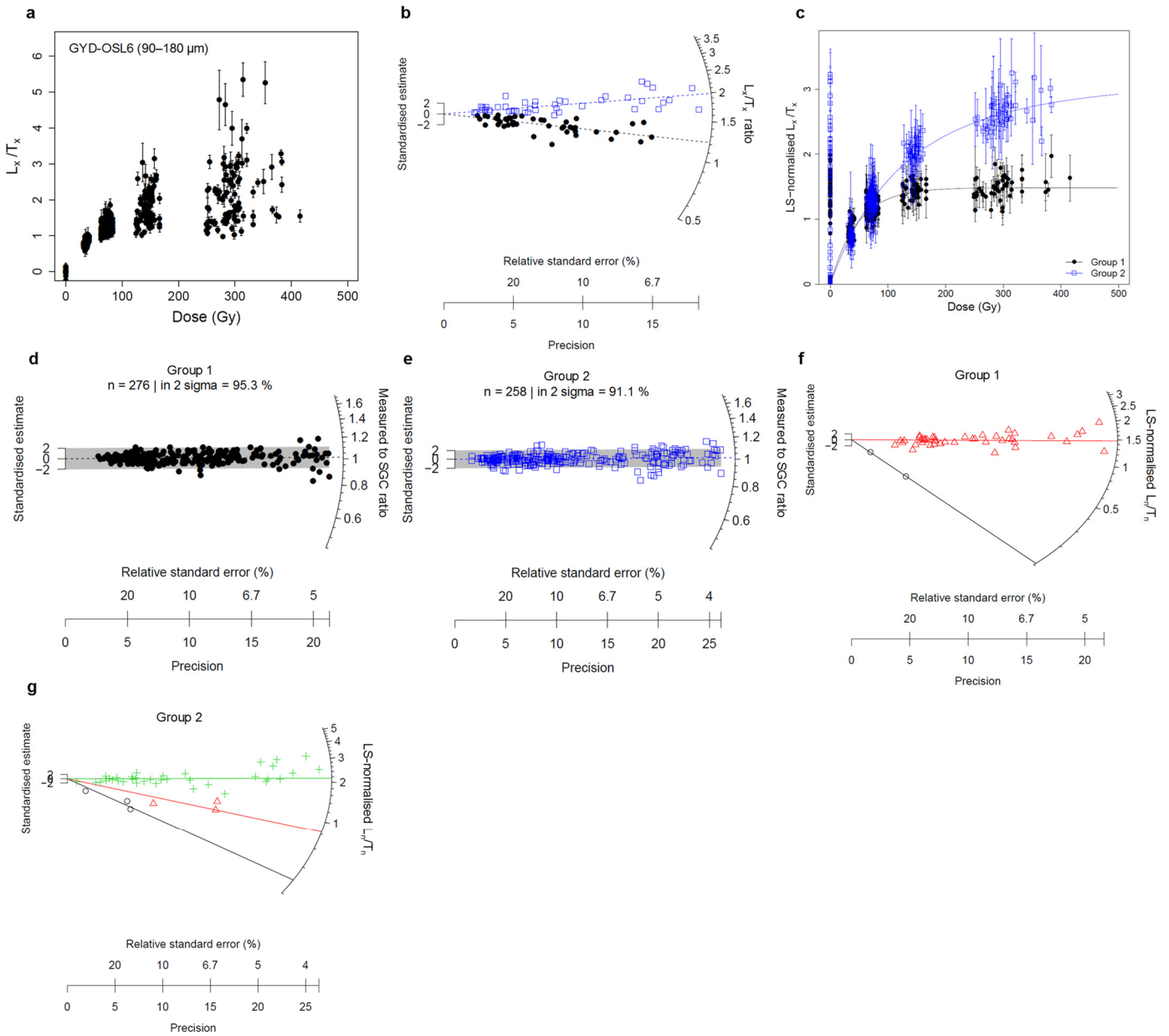ults similar to those described in Supplementary Figs 3g–i. **g,** Radial plots showing the LS-normalised natural signals (L_n/T_n) for group 2; this distribution contains a small number of intrusive grains (open circles) identified as outliers using nMAD, so only the data points shown in filled circles were included in the final weighted mean L_n/T_n value calculated using the CAM.
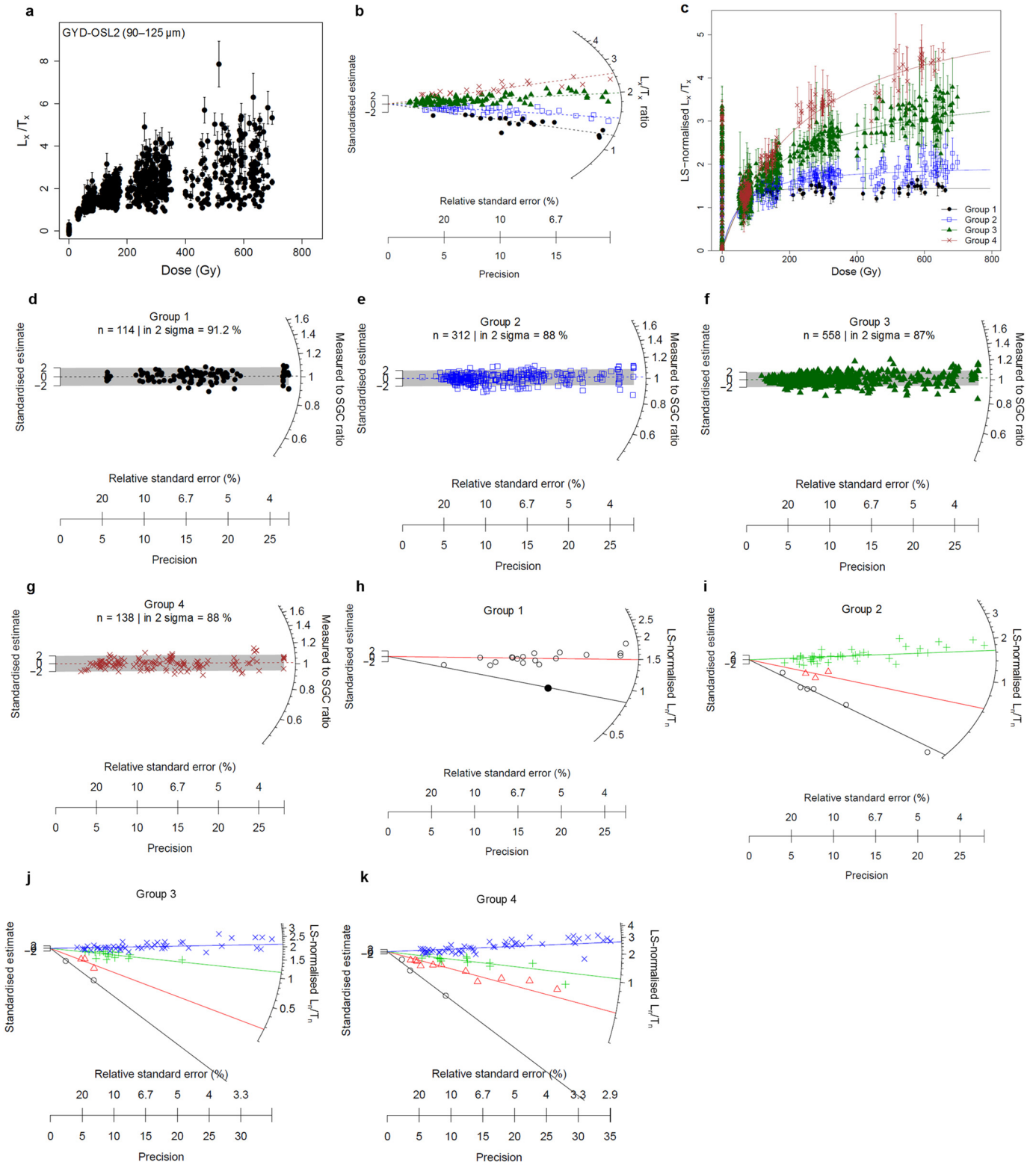
Supplementary Figure 5 | Single-grain measurement results for the 90–125 µm fraction of sample GYD-OSL2. a–c, Results similar to those described in Supplementary Figs 3a–c. **d–g,** Results similar to those described in Supplementary Figs 3d–f. **h–k,** Results similar to those described in Supplementary Figs 3g–i.
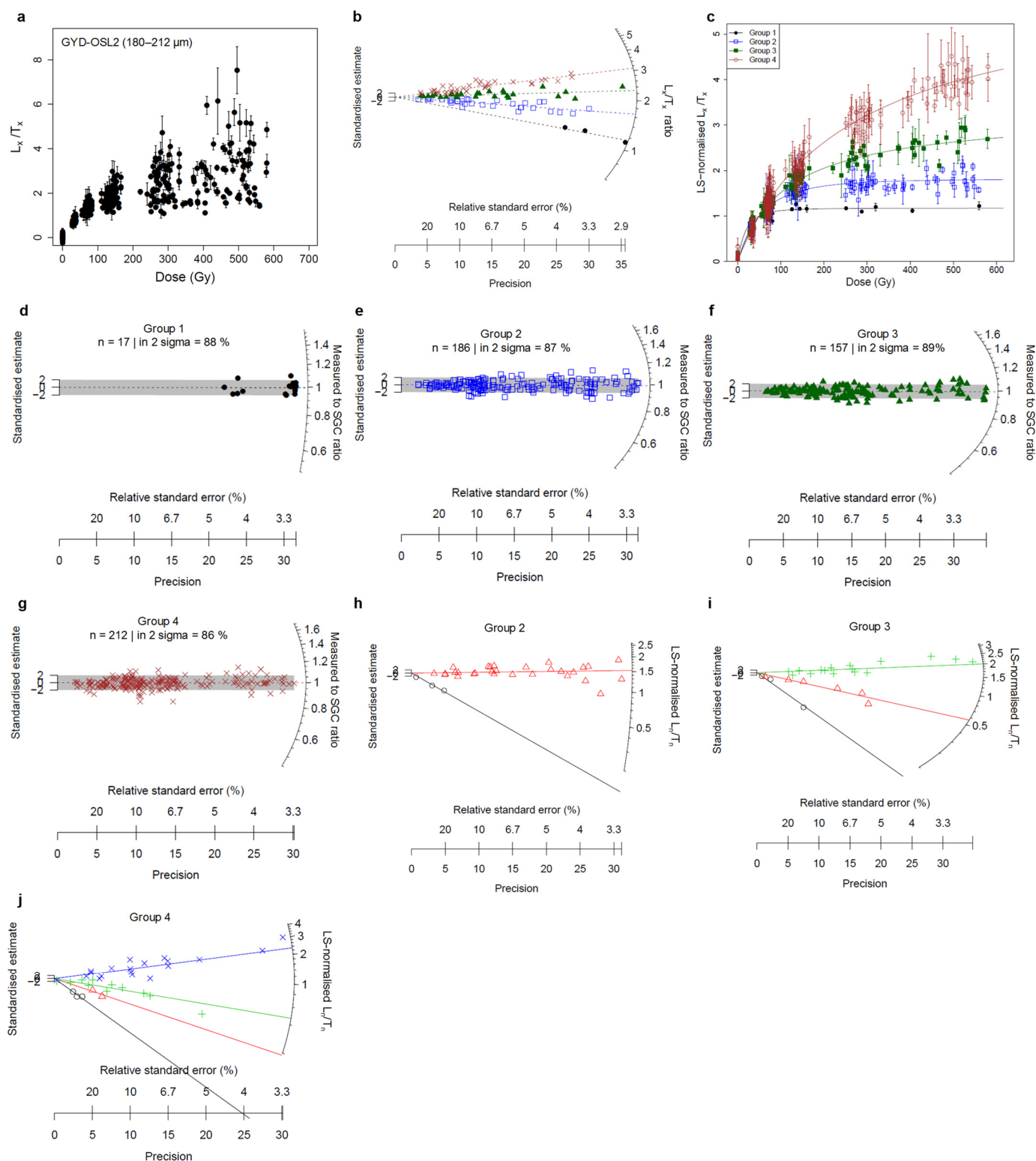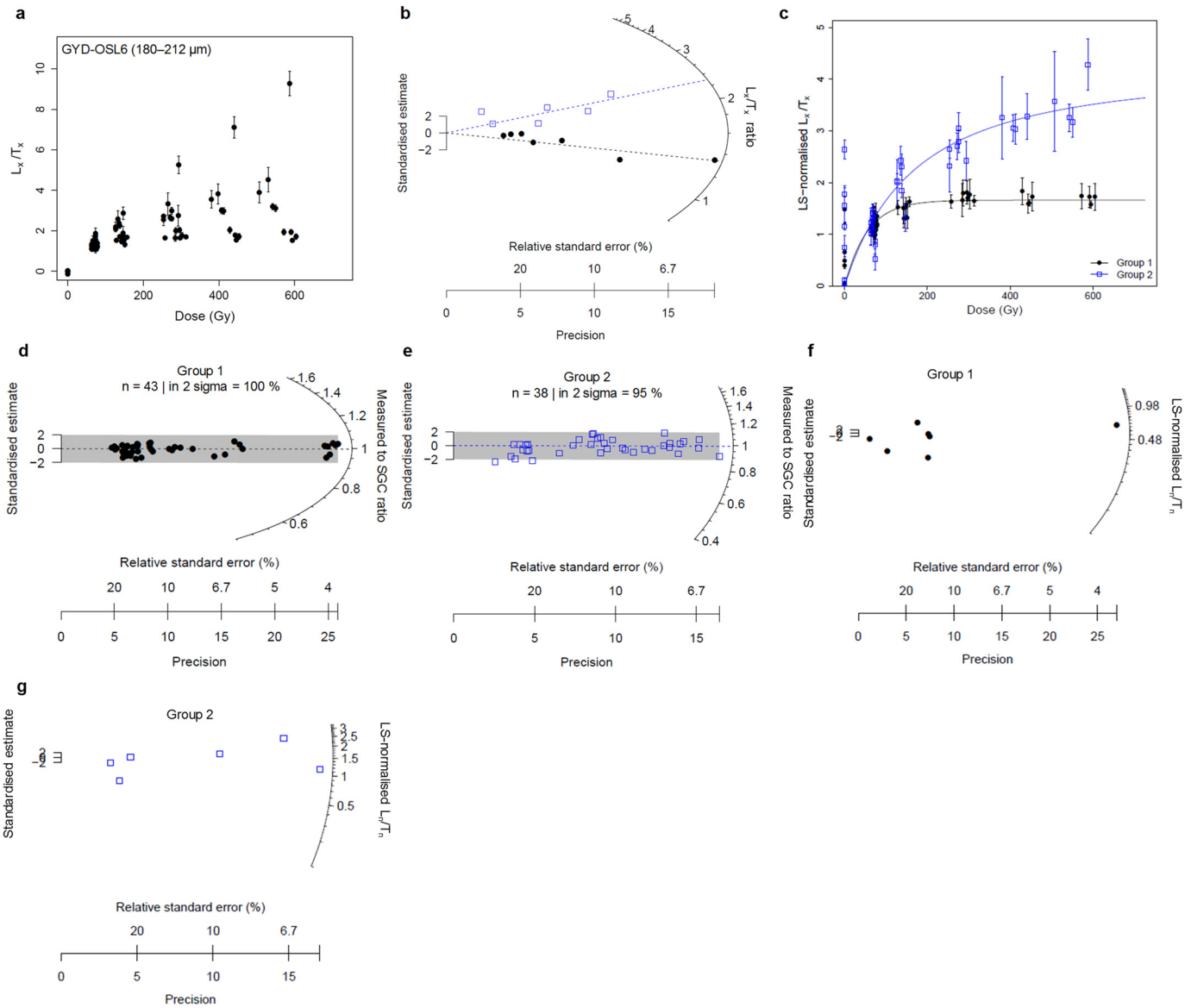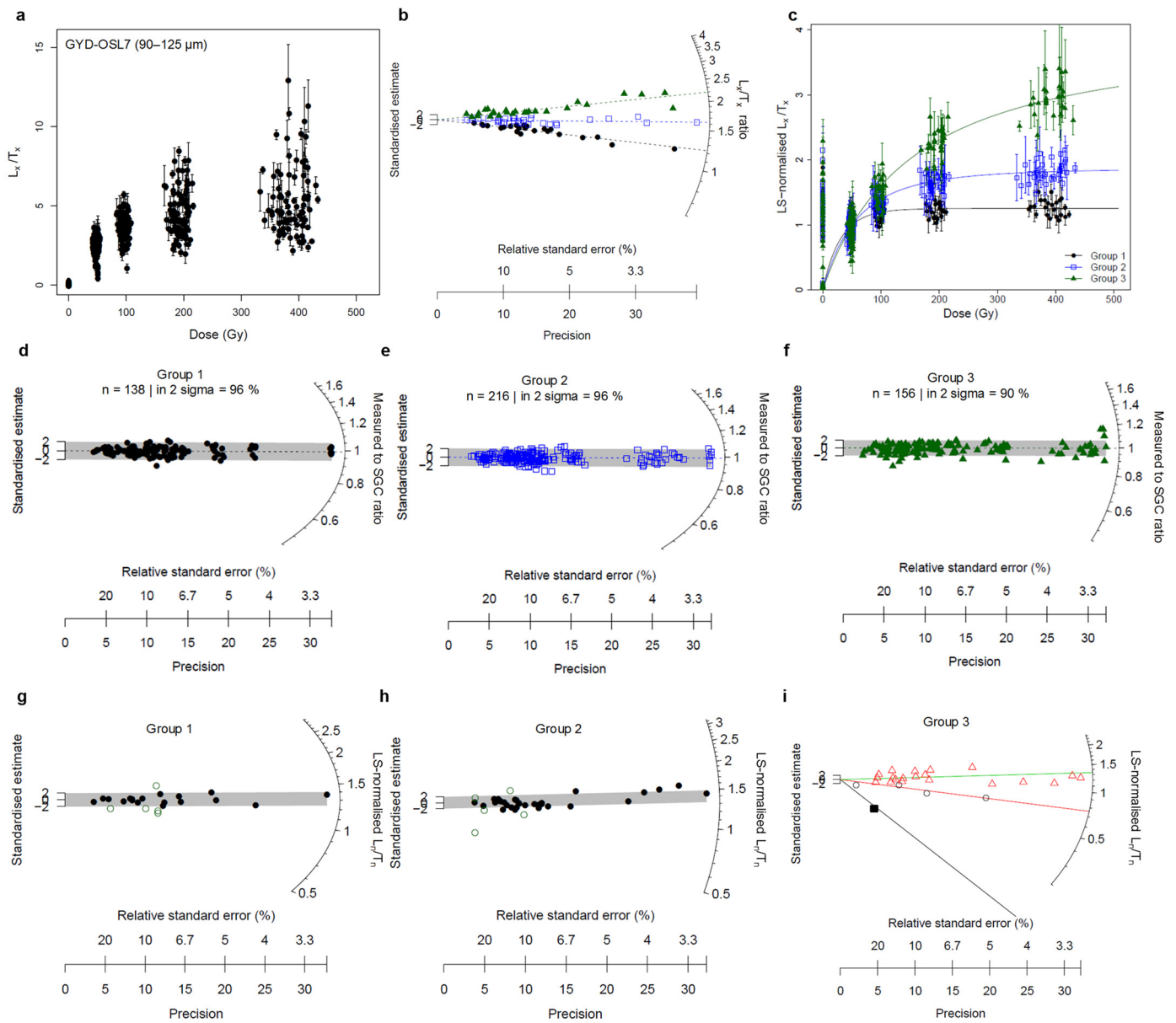
Supplementary Figure 6 | Single-grain measurement results for the 180–212 μm fraction of sample GYD-OSL2. a–c, Results similar to those described in Supplementary Figs 3a–c. **d–g,** Results similar to those described in Supplementary Figs 3d–f. **h–j,** Results similar to those described in Supplementary Figs 3g–i. Note that only 3 grains were identified as group 1 and all are 'modern' grains, so their natural signals are not plotted here.
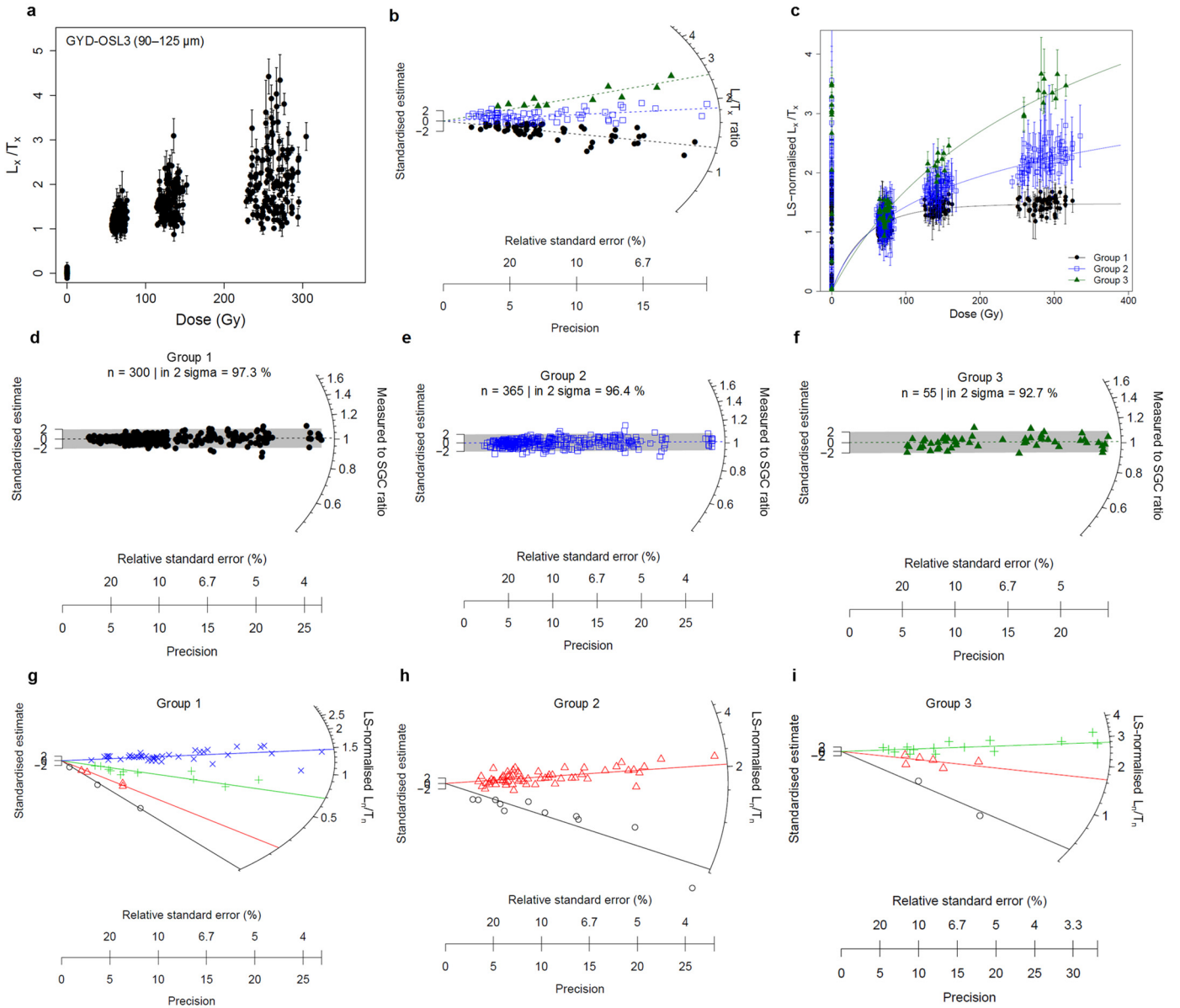
Supplementary Figure 7 | Single-grain measurement results for the 90–125 µm fraction of sample GYD-OSL3. a–c, Results similar to those described in Supplementary Figs 3a–c. **d–f,** Results similar to those described in Supplementary Figs 3d–f. **g–i,** Results similar to those described in Supplementary Figs 3g–i.
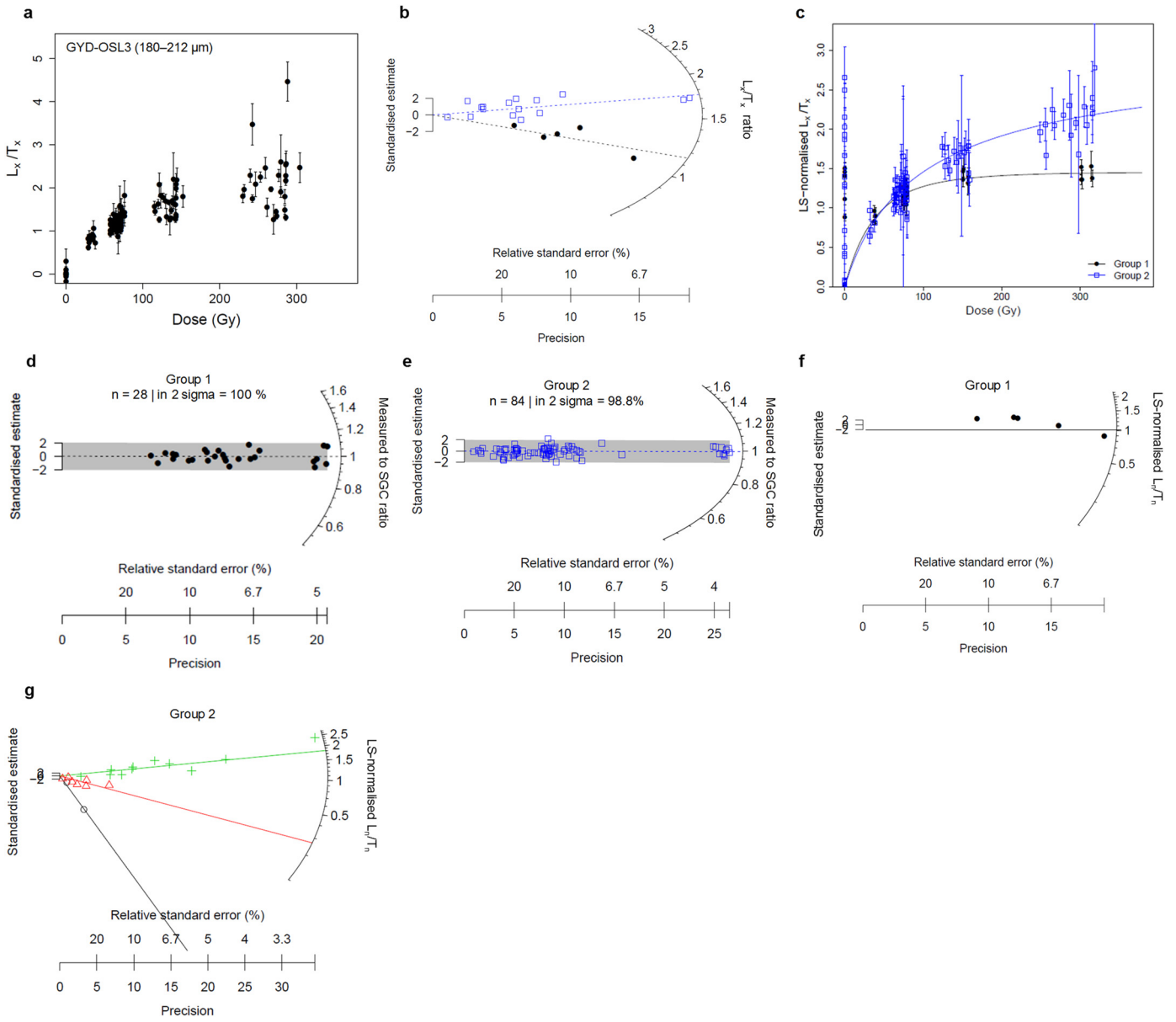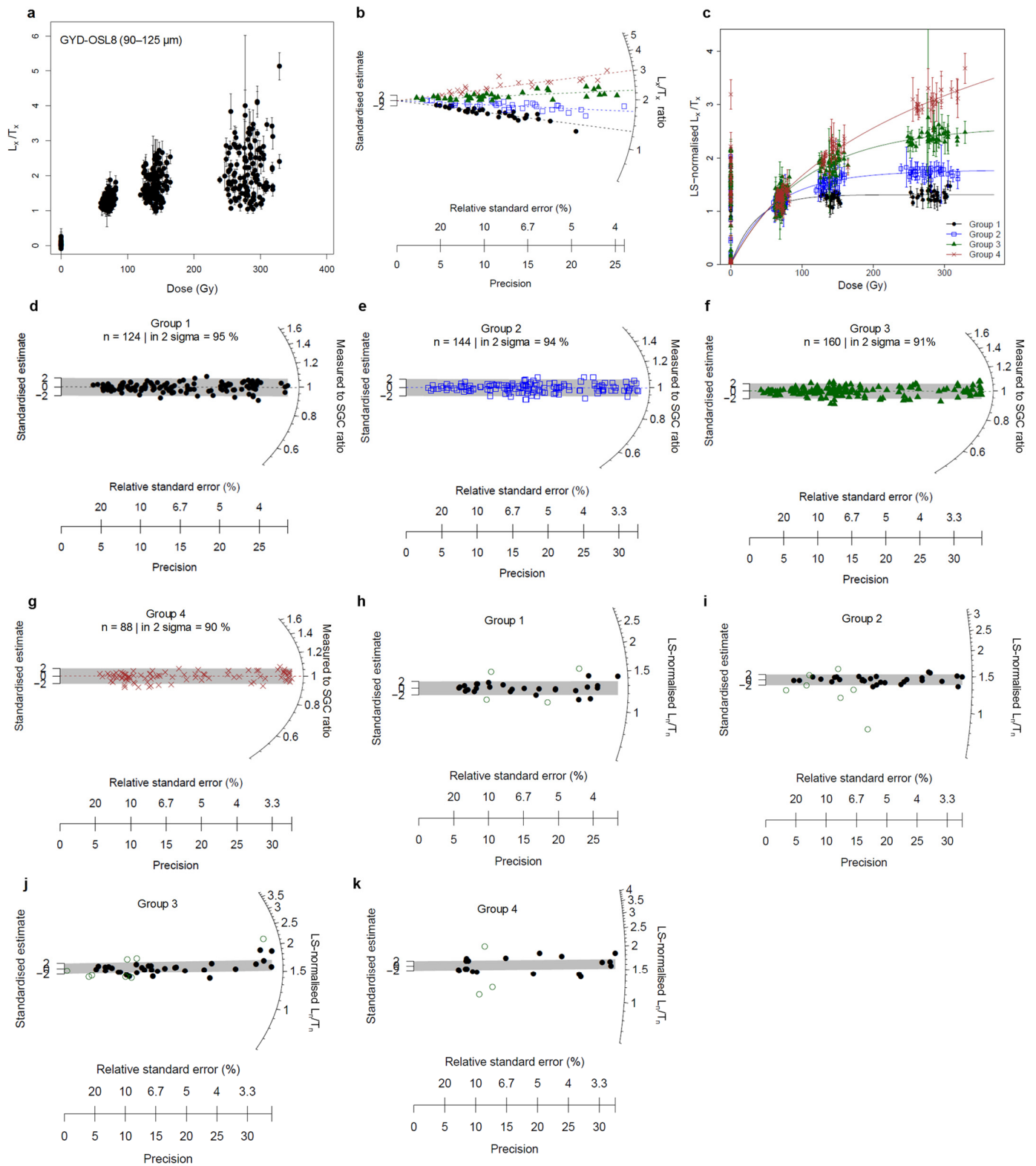
Supplementary Figure 8 | Single-grain measurement results for the 180–212 μm fraction of sample GYD-OSL3. a–c, Results similar to those described in Supplementary Figs 3a–c. **d–e,** Results similar to those described in Supplementary Figs 3d–f. **f–g,** Results similar to those described in Supplementary Figs 3g–i.
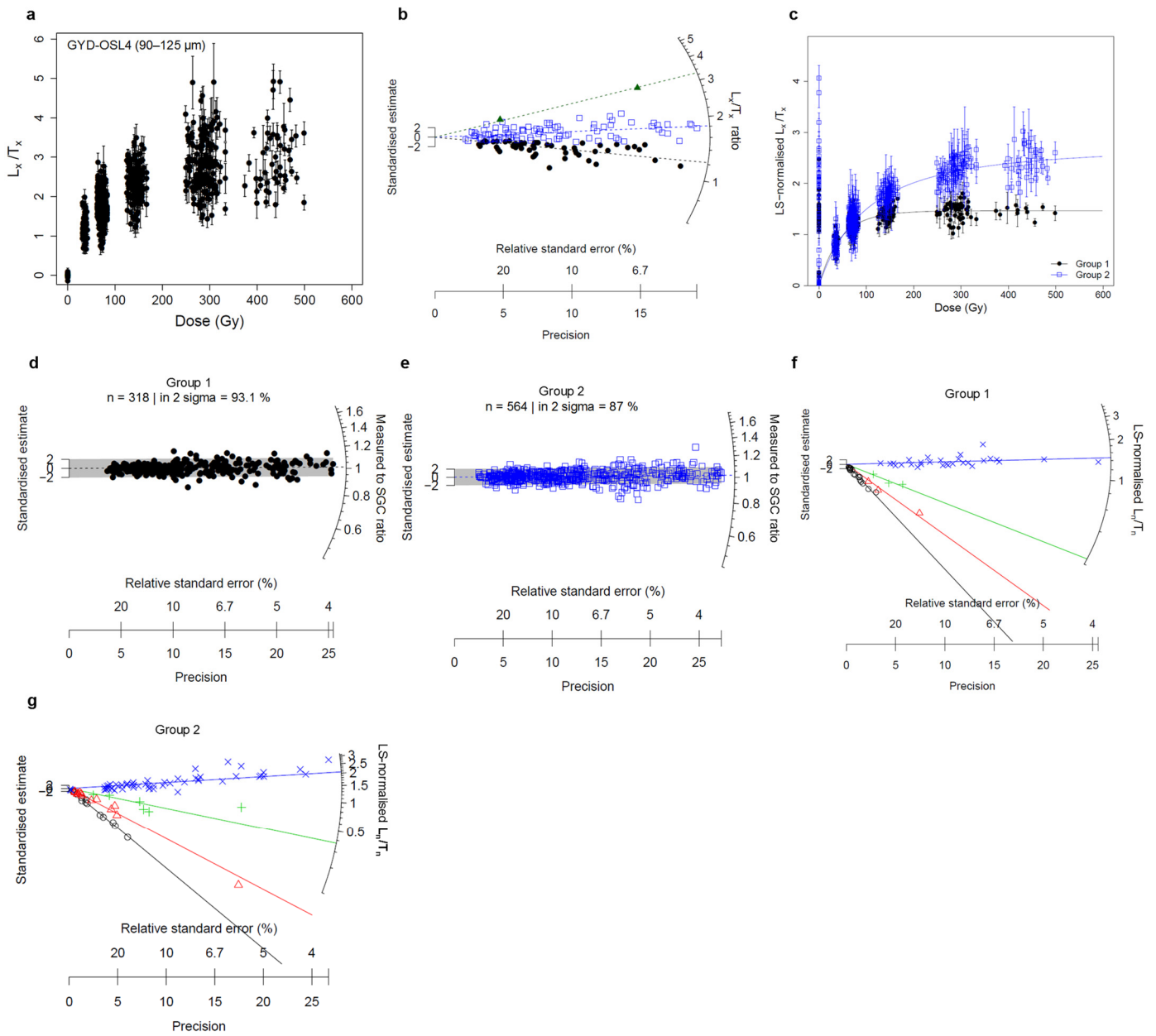
Supplementary Figure 9 | Single-grain measurement results for the 90–125 µm fraction of sample GYD-OSL4. a–c,
Results similar to those described in Supplementary Figs 3a–c. **d–e,** Results similar to those described in Supplementary Figs 3d–
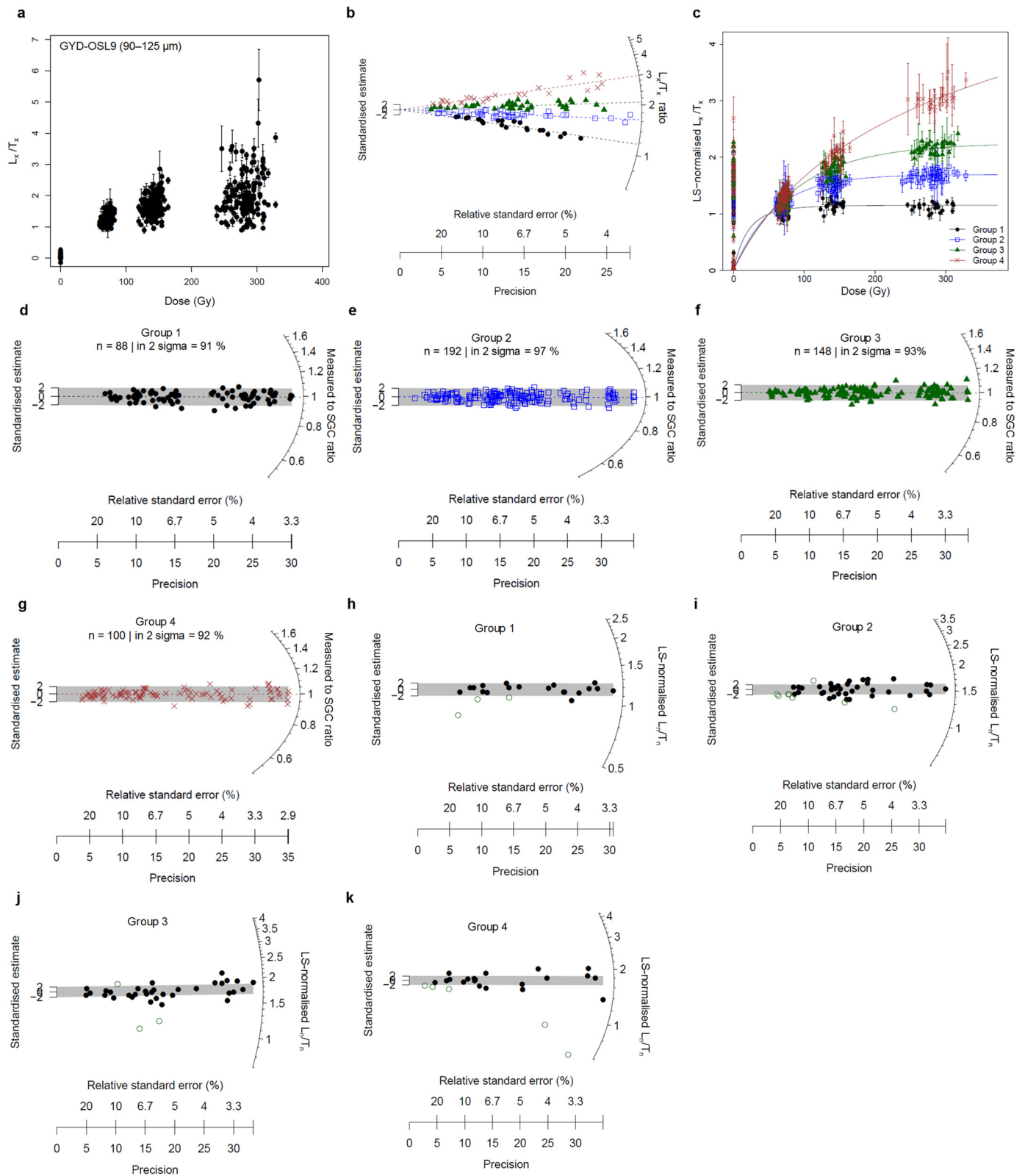f. **f–g**, Results similar to those described in Supplementary Figs 3g–i.

Supplementary Figure 10 | Single-grain measurement results for the 90–180 μm fraction of sample GYD-OSL5. a–c, Results similar to those described in Supplementary Figs 3a–c. **d–f,** Results similar to those described in Supplementary Figs 3d–f. **g,** Results similar to those described in Supplementary Fig. 4g. **h–i,** Results similar to those described in Supplementary Figs 3g–i.
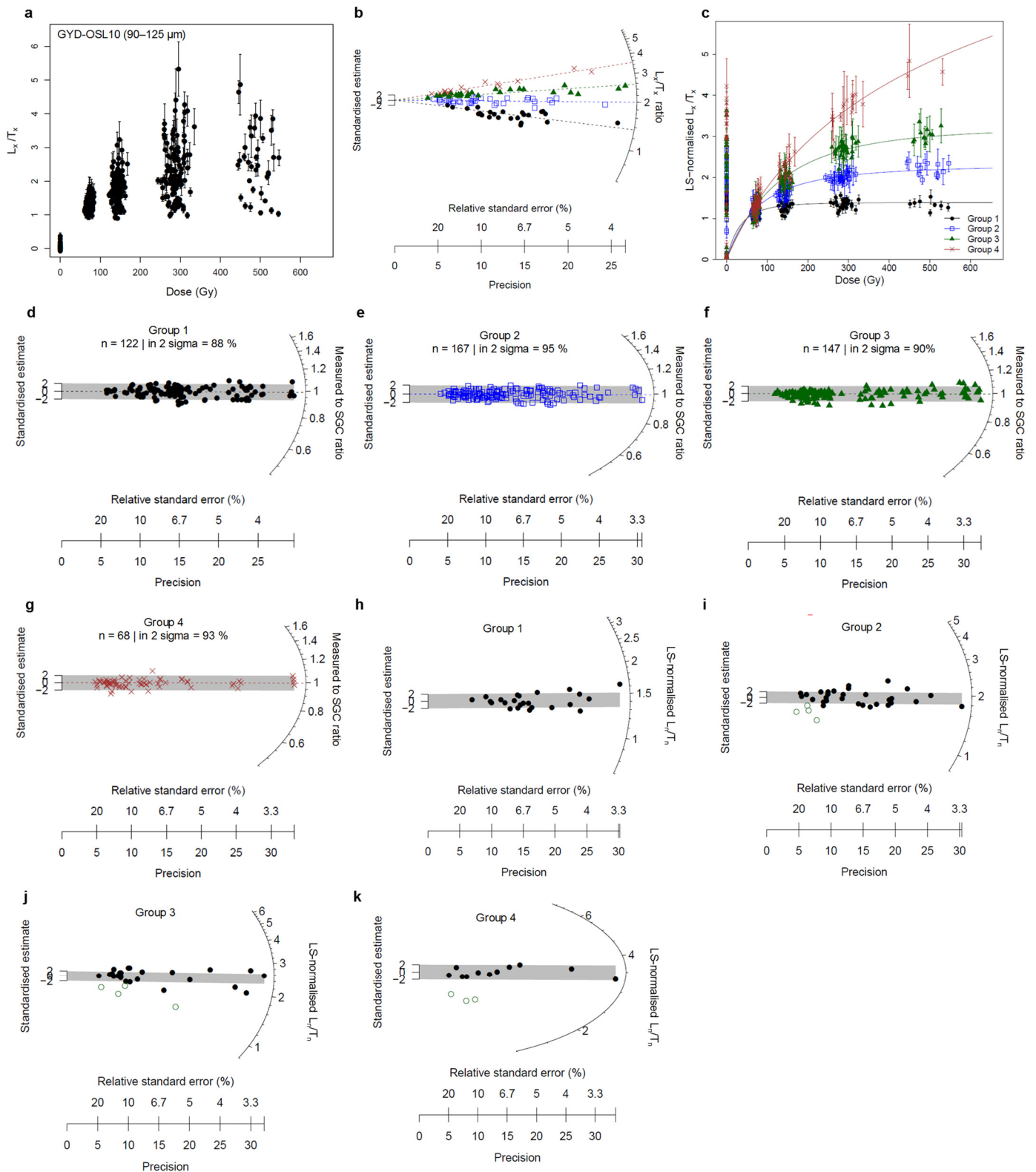
Supplementary Figure 11 | Single-grain measurement results for the 180–212 µm fraction of sample GYD-OSL5. a–c, Results similar to those described in Supplementary Figs 3a–c. **d–f,** Results similar to those described in Supplementary Figs 3d–f. **g–h,** Results similar to those described in Supplementary Figs 3g–i. **i,** Radial plots showing the LS-normalised natural signals (L_n/T_n) for group 3; the data sets of this group are too scattered and too few to apply any age model reliably.
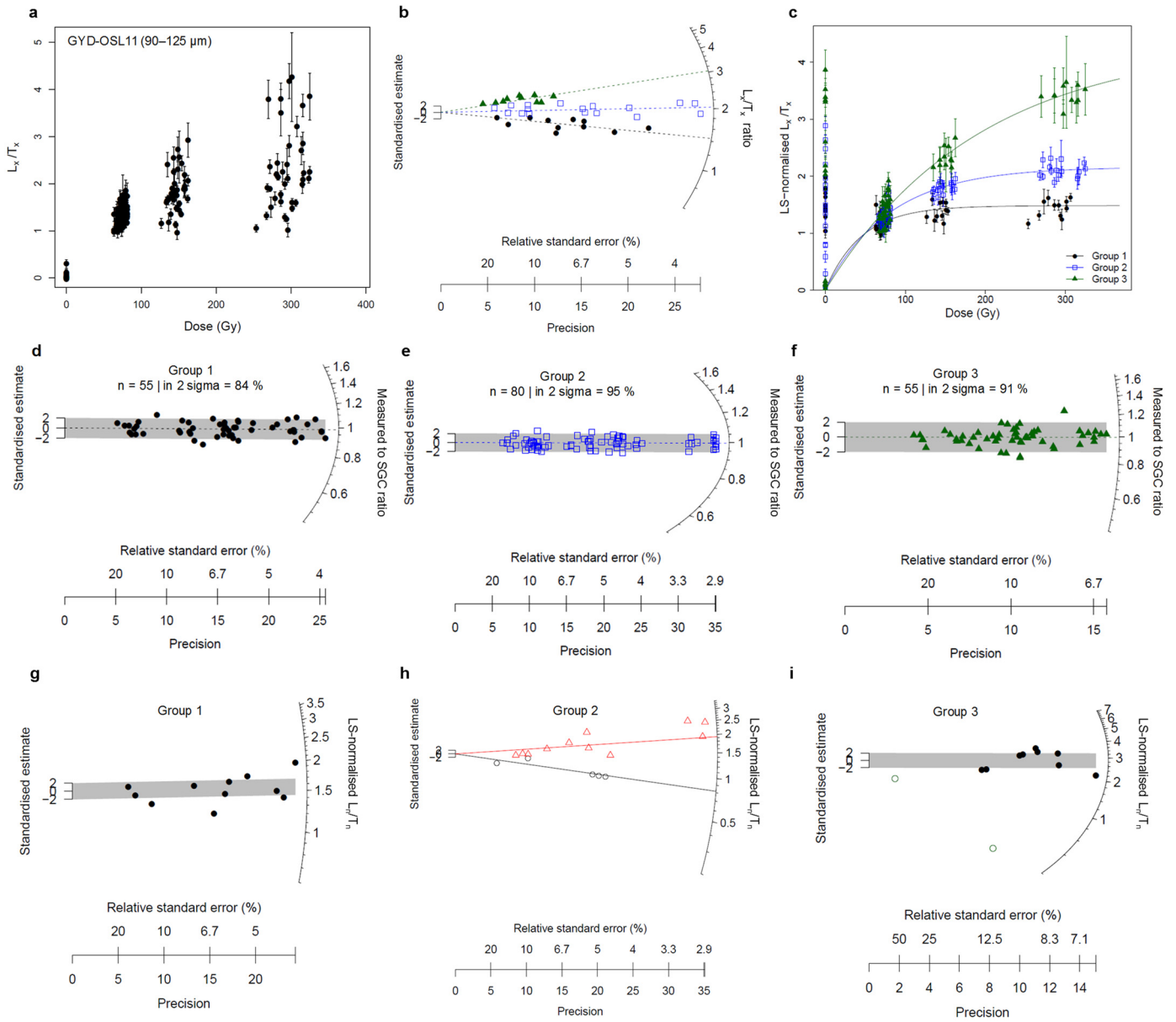
Supplementary Figure 12 | Single-grain measurement results for the 90–180 μm fraction of sample GYD-OSL6. a–c, Results similar to those described in Supplementary Figs 3a–c. **d–e,** Results similar to those described in Supplementary Figs 3d–f. **f–g,** Results similar to those described in Supplementary Figs 3g–i.

Supplementary Figure 13 | Single-grain measurement results for the 180–212 µm fraction of sample GYD-OSL6. a–c, Results similar to those described in Supplementary Figs 3a–c. **d–e,** Results similar to those described in Supplementary Figs 3d–f. **f–g,** Results similar to those described in Supplementary Fig. 11i.
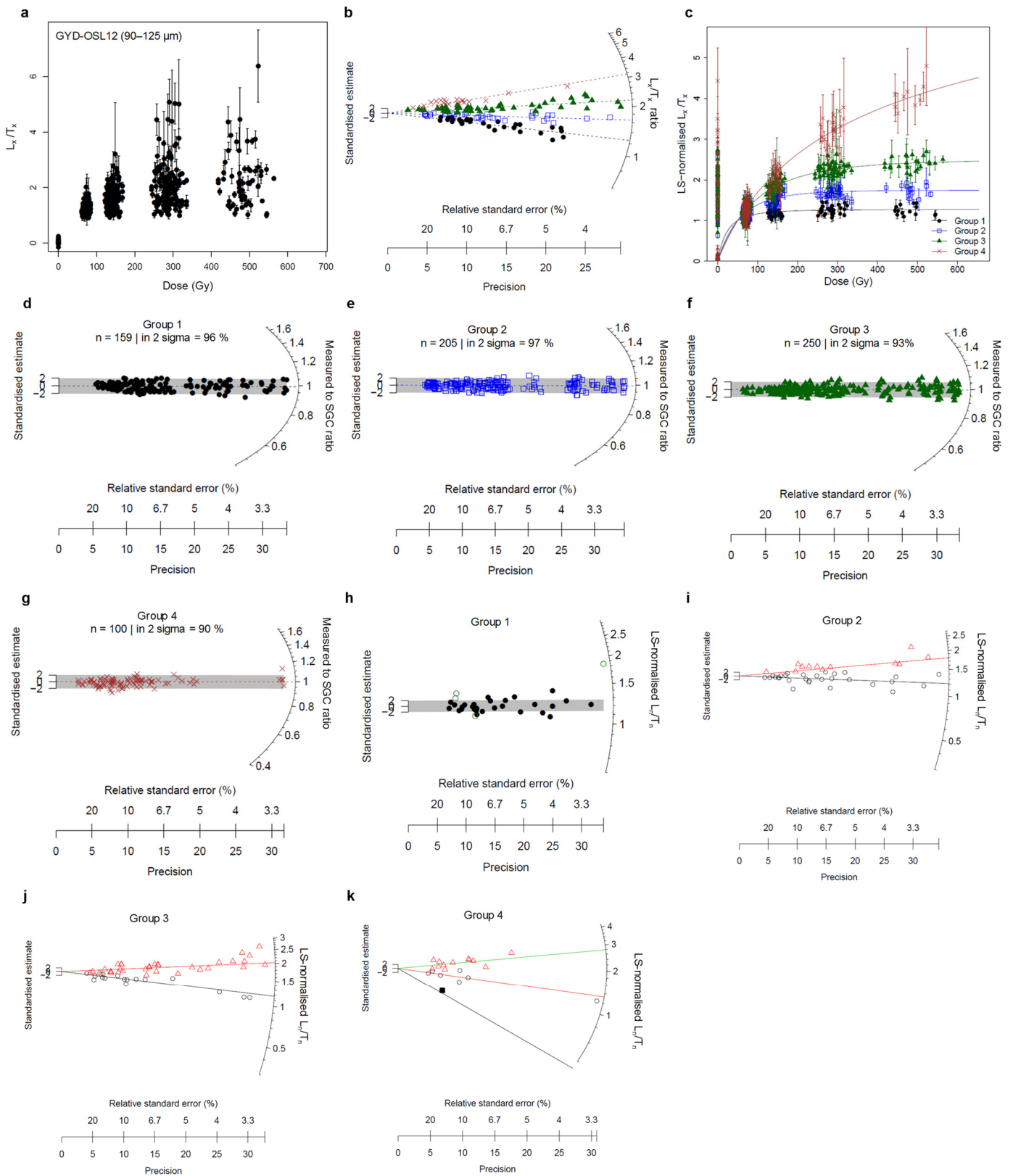
Supplementary Figure 14 | Single-grain measurement results for the 90–125 μm fraction of sample GYD-OSL7. a–c, Results similar to those described in Supplementary Figs 3a–c. **d–f,** Results similar to those described in Supplementary Figs 3d–f. **g–h,** Results similar to those described in Supplementary Fig. 4g. **i,** Results similar to those described in Supplementary Figs 3g-i.

Supplementary Figure 15 | Single-grain measurement results for the 90–125 µm fraction of sample GYD-OSL8. a–c, Results similar to those described in Supplementary Figs 3a–c. **d–g,** Results similar to those described in Supplementary Figs 3d–f. **h–k,** Results similar to those described in Supplementary Fig. 4g.
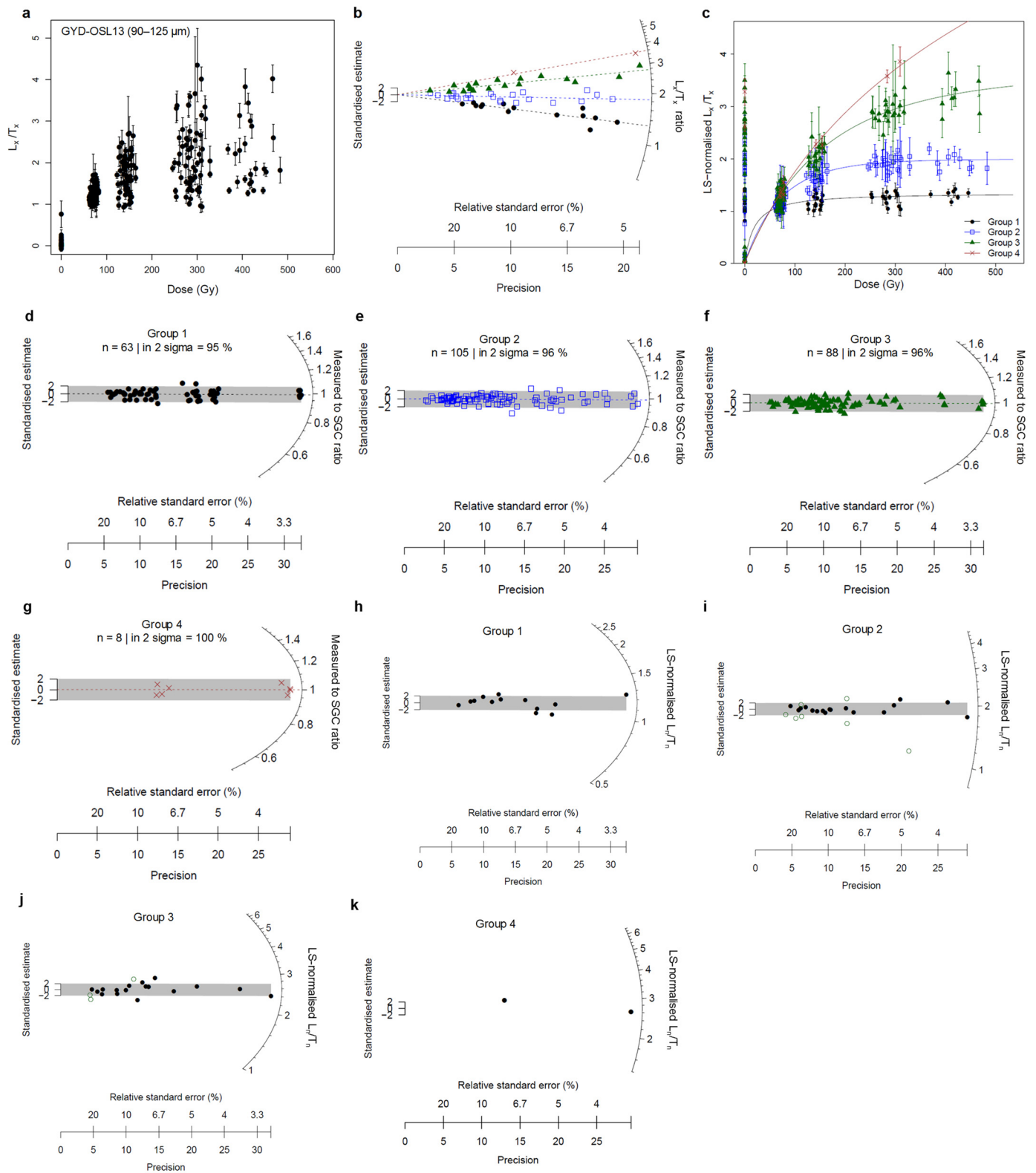
Supplementary Figure 16 | Single-grain measurement results for the 90–125 μm fraction of sample GYD-OSL9. a–c, Results similar to those described in Supplementary Figs 3**a–c**. **d–g,** Results similar to those described in Supplementary Figs 3**d–f**. **h–k,** Results similar to those described in Supplementary Fig. 4g.

Supplementary Figure 17 | Single-grain measurement results for the 90–125 µm fraction of sample GYD-OSL10. a–c, Results similar to those described in Supplementary Figs 3a–c. **d–g,** Results similar to those described in Supplementary Figs 3d–f. **h–k,** Results similar to those described in Supplementary Fig. 4g.

Supplementary Figure 18 | Single-grain measurement results for the 90–125 μm fraction of sample GYD-OSL11. a–c,
Results similar to those described in Supplementary Figs 3a–c. **d–f,** Results similar to those described in Supplementary Figs 3d–f. **g–i,** Results similar to those described in Supplementary Figs 3g–i and 4g.

Supplementary Figure 19 | Single-grain measurement results for the 90–125 µm fraction of sample GYD-OSL12. a–c, Results similar to those described in Supplementary Figs 3a–c. **d–g,** Results similar to those described in Supplementary Figs 3d–f. **h–k,** Results similar to those described in Supplementary Figs 3g–i and 4g.

Supplementary Figure 20 | Single-grain measurement results for the 90–125 μm fraction of sample GYD-OSL13. a–c, Results similar to those described in Supplementary Figs 3a–c. **d–g,** Results similar to those described in Supplementary Figs 3d–f. **h–j,** Results similar to those described in Supplementary Fig. 4g. **k,** Results similar to those described in Supplementary Figs 11i.
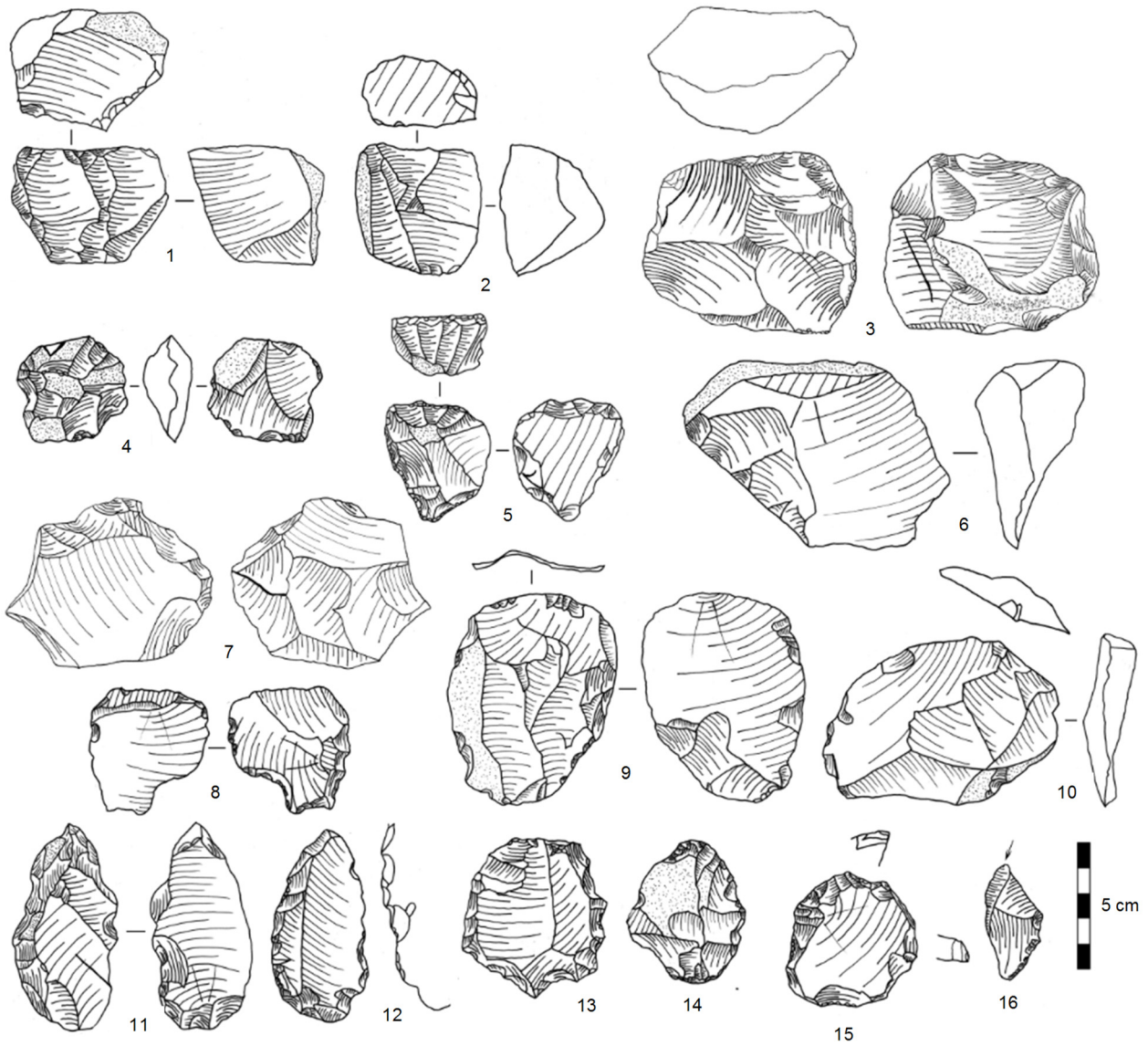
Supplementary Figure 21 | Line drawings of selected non-Levallois artefacts. 1, Single platform core. **2,** Double platform core. **3–4,** Discoid cores. **5,** Blade core. **6, 7,** Truncated facetted pieces. **8,** Kombewa flake. **9, 10, 14,** Flakes. **11 and 13,** Denticulates. **12,** Convergent scraper. **15,** Double scrapers. **16,** Burin. The photos of these artefacts are shown in Supplementary Fig. 22.
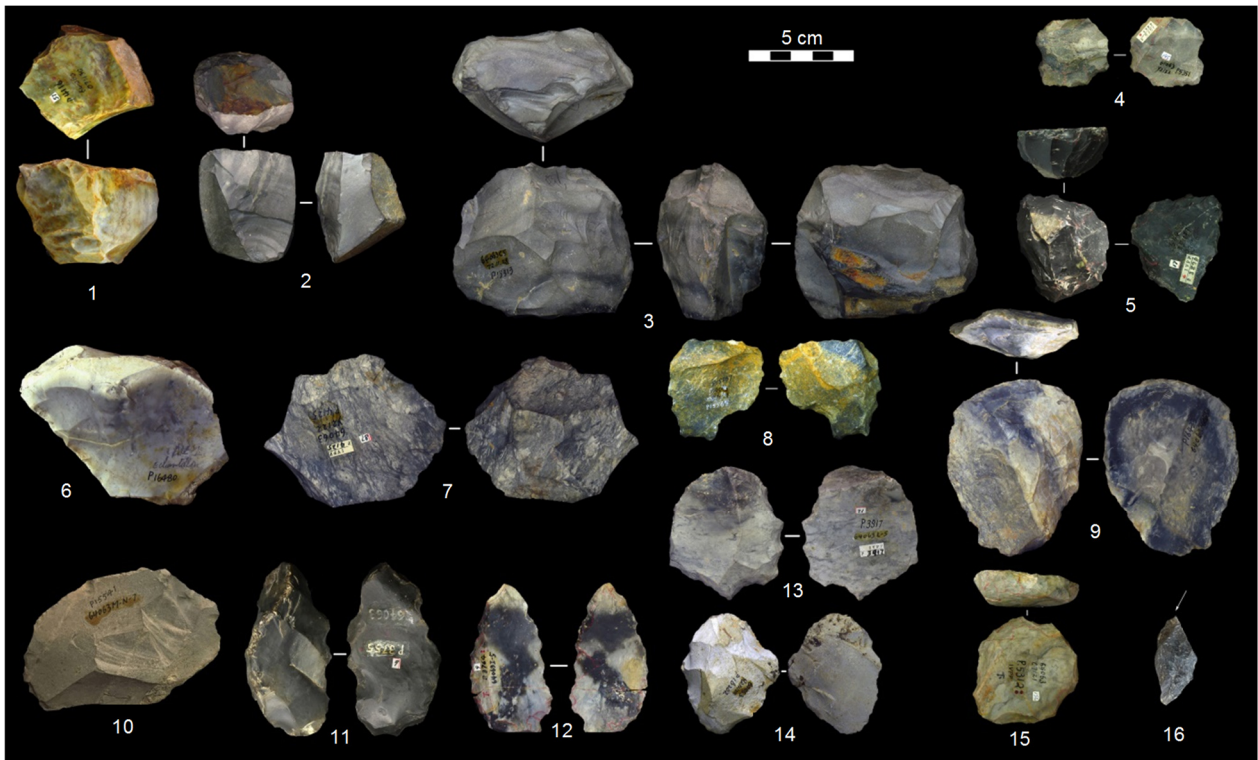
Supplementary Figure 22 | Photos of selected non-Levallois artefacts. 1, Single platform core. **2,** Double platform core. **3–4,** Discoid cores. **5,** Blade core. **6, 7,** Truncated facetted pieces. **8,** Kombewa flake. **9, 10, 14,** Flakes. **11 and 13,** Denticulates. **12,** Convergent scraper. **15,** Double scrapers. **16,** Burin. The line drawings of these artefacts are shown in Supplementary Fig. 21.
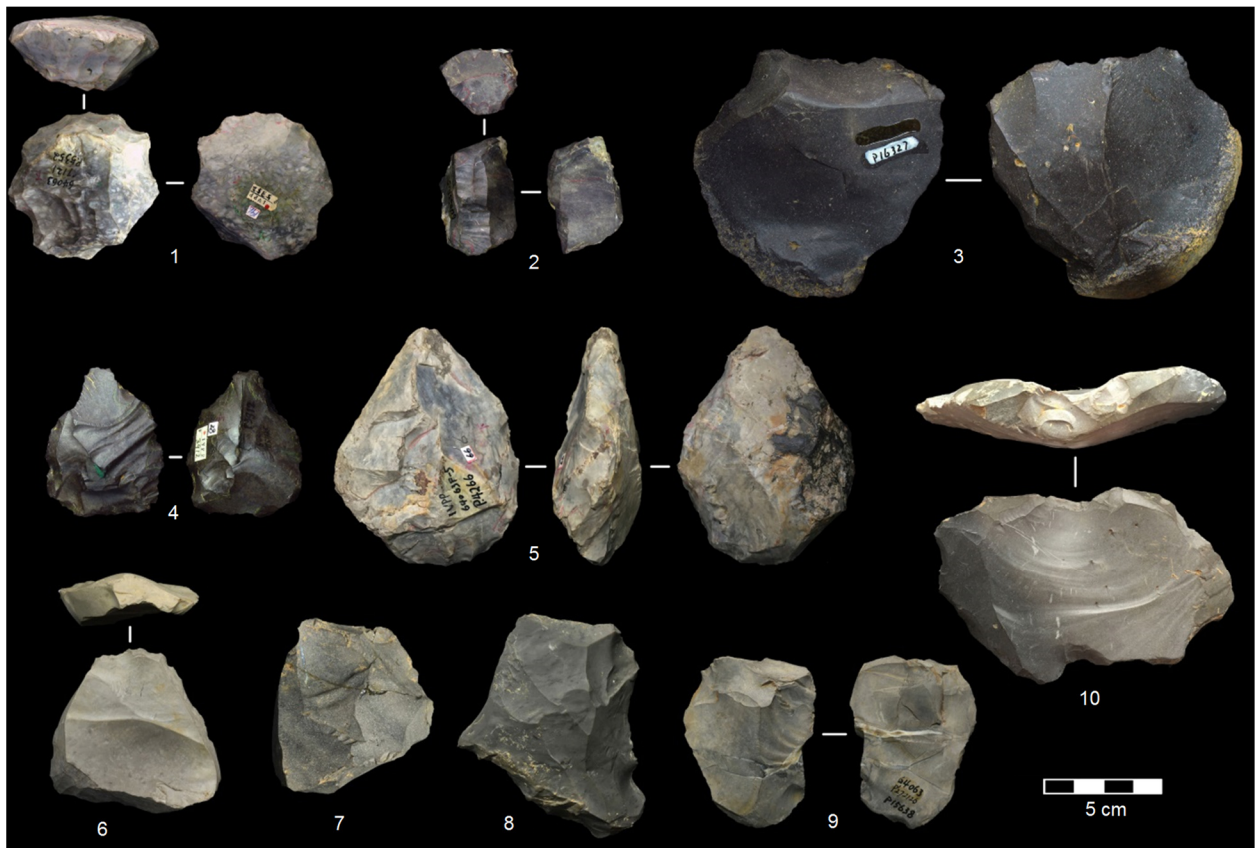
Supplementary Figure 23 | Photos of selected non-Levallois artefacts. 1–2, Blade cores. **3,** Truncated facetted pieces. **4–5,** Bifaces. **6–10,** Flakes.

Supplementary Figure 24 | Photos of selected non-Levallois artefacts. 1–5, 9, Scrapers with retouched edges that resemble tools found in Mousterian industries. **6, 10, 11,** Convergent scrapers. **7, 8, 19,** Double scrapers. **12–14,** Denticulates. **15–17,** Borers. **18,** Notch.

References

1   Zhang, M. L. *et al.* The record of paleoclimatic change from stalagmites and the determination of termination II in the south of Guizhou Province, China. *Science in China Series D: Earth Sciences* **47**, 1-12, doi:10.1007/BF03028857 (2004).

2   Li, Y. X. & Wen, B. H. *Guanyindong—A Lower Paleolithic Site at Qianxi County, Guizhou Province*. (Cultural Relics Publishing House, 1986).

3   Pei, W. C., Yuan, C. S., Lin, Y. P., Chang, Y. Y. & Tsao, C. T. Discovery of Paleolithic chert artifacts in Kuan-Yin-Tung Cave in Chien-Hsi-Hsien of Kweichow Province. *Vertebrat Palasiatic* **9**, 270-279 (1965).

4   Yuan, S. X., Chen, T. M. & Gao, S. J. Uranium series chronological sequence of some Paleolithic sites in South China. *Acta Anthropologica Sinica* **5**, 179-190 (1986).

5   Grün, R., Eggins, S., Kinsley, L., Moseley, H. & Sambridge, M. Laser ablation U-series analysis of fossil bones and teeth. *Palaeogeogr. Palaeoclimatol. Palaeoecol.* **416**, 150-167, doi:https://doi.org/10.1016/j.palaeo.2014.07.023 (2014).

6   Shen, G. J. & Jin, L. H. U-series dating of speleothem samples from Guanyindong Cave at Qianxi County, Guizhou Province. *Acta Anthropologica Sinica* **11**, 93-100 (1992).

7   Hovers, E. *The lithic assemblages of Qafzeh Cave*. (Oxford University Press, 2009).

8   Perpère, M. Apport de la typométrie à la définition des éclats Levallois: l'exemple d'Ault. *Bulletin de la Société préhistorique française*, 115-118 (1986).

9   Boëda, E. Approche de la variabilité des systèmes de production lithique des industries du paléolithique inférieure et moyen: chronique d'une variabilité attendue. *Techniques Culture* **17–18**, 31–79 (1991).

10   Freeman, L. G. in *Paleoanthropology in the People's Republic of China: A Trip Report of the American Paleoanthropology Delegation: Submitted to the Committee on Scholarly Communication with the People's Republic of China* Vol. 4 (eds William White Howells & Patricia Jones Tsuchitani) 79-114 (National Academies, 1977).

11   Li, Y., Hou, Y. & Boëda, E. Mode de débitage and technical cognition of hominids at the Guanyindong site. *Chinese Science Bulletin* **54**, 3864-3871 (2009).

12   Gao, X. Paleolithic Cultures in China: Uniqueness and Divergence. *Curr Anthrop* **54**, S358-S370, doi:10.1086/673502 (2013).

13   Bar-Yosef, O. & Van Peer, P. The Chaîne Opératoire Approach in Middle Paleolithic Archaeology. *Curr Anthrop* **50**, 103-131, doi:10.1086/592234 (2009).

14   Monnier, G. F. & Missal, K. Another Mousterian Debate? Bordian facies, *chaîne op eratoire* technocomplexes, and patterns of lithic variability in the western European Middle and Upper Pleistocene. *Quaternary International* **350**, 59-83 (2014).

15   Boëda, E. *Approche technologique du concept Levallois et évaluation de son champ d'application: étude de trois gisement saaliens et weichseliens de la France septentrionale*, Paris 10, (1986).

16   Dibble, H. L. Biache Saint-Vaast, Level IIA: A comparison of analytical approaches. *The definition and interpretation of Levallois technology*, 93-116 (1995).

17   Mathias, C. After the Lower Palaeolithic: Lithic ramification in the early Middle Palaeolithic of Orgnac 3, layer 2 (Ardèche, France). *Quaternary International* **411**, 193-201, doi:https://doi.org/10.1016/j.quaint.2016.01.033 (2016).

18   Moncel, M.-H. *et al.* The Emergence of Neanderthal Technical Behavior: New Evidence from Orgnac 3 (Level 1, MIS 8), Southeastern France. *Curr Anthrop* **52**, 37-75, doi:10.1086/658179 (2011).

19   Li, Y. H. *Tehnological study of lithic industry of the Guanyindong site, Guizhou province, south-west of China* PhD thesis, The Institute of Vertebrate Paleontology and Paleoanthropology, Chinese Academy of Sciences, (2009).

20   Bar-Yosef, O. & Kuhn, S. L. The big deal about blades: Laminar technologies and human evolution. *Amer Anthrop* **101**, 322-338 (1999).

21   Dibble, H., L. & McPherron, S., P. The missing Mousterian. *Curr Anthrop* **47**, 777 (2006).

22   Marwick, B., Clarkson, C., O'Connor, S. & Collins, S. Early modern human lithic technology from Jerimalai, East Timor. *J Hum Evol* **101**, 45-64 (2016).

23   Dibble, H. The Mousterian Industry from Bisitun Cave (Iran). *Paleorient* **10** (1984).

24   Brantingham, P. J., Olsen, J. W., Rech, J. A. & Krivoshapkin, A. I. Raw Material Quality and Prepared Core Technologies in Northeast Asia. *J Archaeol Sci* **27**, 255-271 (2000).

25   Shimelmitz, R. & Kuhn, S. L. The toolkit in the core: There is more to Levallois production than predetermination. *Quatern Int*, doi:https://doi.org/10.1016/j.quaint.2017.08.011 (2017).

26   Wang, H. & Song, M. Ckmeans. 1d. dp: optimal k-means clustering in one dimension by dynamic programming. *The R journal* **3**, 29 (2011).

27   Moore, M. W. The tula adze: Manufacture and purpose. *Antiquity* **78**, 61-73, doi:10.1017/S0003598X00092930 (2004).

28   Leader, G., Abdolahzadeh, A., Lin, S. C. & Dibble, H. L. The effects of platform beveling on flake variation. *Journal of Archaeological Science: Reports* **16**, 213-223, doi:https://doi.org/10.1016/j.jasrep.2017.09.026 (2017).

29   Watanabe, T. & Kanazawa, M. Observations on the melt-off pores of sintered Al-5%Cu alloy compacts by the use of scanning electron microscope. *Journal of the Japan Society of Powder and Powder Metallurgy* **20**, 87-88, doi:10.2497/jjspm.20.87 (1973).

30   Chiotti, L., Dibble, H. L., Olszewski, D. I., McPherron, S. P. & Schurmans, U. A. Middle Palaeolithic lithic technology from the western high desert of Egypt. *J Field Archaeol* **34**, 307-318, doi:10.1179/009346909791070862 (2009).

31   Herries, A. I. R. A Chronological Perspective on the Acheulian and Its Transition to the Middle Stone Age in Southern Africa: The Question of the Fauresmith. *International Journal of Evolutionary Biology* **2011**, 25, doi:10.4061/2011/961401 (2011).

32   Porat, N. *et al.* New radiometric ages for the Fauresmith industry from Kathu Pan, southern Africa: Implications for the Earlier to Middle Stone Age transition. *J Archaeol Sci* **37**, 269-283, doi:https://doi.org/10.1016/j.jas.2009.09.038 (2010).

33   Tryon, C. A. & Faith, J. T. Variability in the Middle Stone Age of Eastern Africa. *Curr Anthropol* **54**, S234-S254, doi:10.1086/673752 (2013).

34   Brown, F. H. & Fuller, C. R. Stratigraphy and tephra of the Kibish Formation, southwestern Ethiopia. *J Hum Evol* **55**, 366-403, doi:https://doi.org/10.1016/j.jhevol.2008.05.009 (2008).

35   Grün, R. *et al.* Direct dating of Florisbad hominid. *Nature* **382**, 500-501 (1996).

36   Douze, K. & Delagnes, A. The pattern of emergence of a Middle Stone Age tradition at Gademotta and Kulkuletti (Ethiopia) through convergent tool and point technologies. *J Hum Evol* **91**, 93-121, doi:https://doi.org/10.1016/j.jhevol.2015.11.006 (2016).

37   Tryon, C. Middle Stone Age Lithic Technology of the Kapthurin Formation (Kenya). *Curr Anthropol* **47**, 367-375, doi:10.1086/503066 (2006).

38   Hawkins, A. L. *et al.* New research on the prehistory of the escarpment in Kharga Oasis, Egypt. *NYAME AKUMA* **55**, 8-14 (2001).

39   Van Peer, P. *et al.* The Early to Middle Stone Age Transition and the Emergence of Modern Human Behaviour at site 8-B-11, Sai Island, Sudan. *J Hum Evol* **45**, 187-193, doi:https://doi.org/10.1016/S0047-2484(03)00103-9 (2003).

40   Buraczynski, J. & Butrym, J. in *Loess and Environment* Vol. 9 (ed M. Pesci) 81-94 (1987).

41   Falguères, C. *et al.* The Lower Acheulian site of Ambrona, Soria (Spain): ages derived from a combined ESR/U-series model. *J Archaeol Sci* **33**, 149-157, doi:https://doi.org/10.1016/j.jas.2005.07.006 (2006).

42   Santonja, M. & Villa, P. The Lower Paleolithic of Spain and Portugal. *J World Prehist* **4**, 45-94, doi:10.1007/BF00974819 (1990).

43   Falguères, C. *et al.* Earliest humans in Europe: the age of TD6 Gran Dolina, Atapuerca, Spain. *J Hum Evol* **37**, 343-352, doi:https://doi.org/10.1006/jhev.1999.0326 (1999).

44   Fontana, F. *et al.* Widespread diffusion of technical innovations around 300,000 years ago in Europe as a reflection of anthropological and social transformations? New comparative data from the western Mediterranean sites of Orgnac (France) and Cave dall'Olio (Italy). *J Anthropol Archaeol* **32**, 478-498, doi:http://dx.doi.org/10.1016/j.jaa.2013.08.003 (2013).

45   Carbonell, E. & Rodríguez, X. P. El Paleolítico Inferior En Cataluña. *VELEIA* **24-25**, 331-343 (2008).

46   Falguères, C., Bahain, J.-J. & Saleki, H. U-Series and ESR Dating of Teeth from Acheulian and Mousterian Levels at La Micoque (Dordogne, France). *J Archaeol Sci* **24**, 537-545, doi:http://dx.doi.org/10.1006/jasc.1996.0137 (1997).

47   Tuffreau, A. *L'Acheuléen dans la vallée de la Somme et Paléolithique moyen dans le Nord de la France: données récentes*. (Centre d'études et de recherches préhistoriques, Université des sciences et technologies de Lille, 2001).

48   Michel, V. *et al.* Application of U/Th and ⁴⁰Ar/³⁹Ar dating to orgnac 3, a Late Acheulean and Early Middle Palaeolithic site in Ardèche, France. *Plos One* **8**, doi:10.1371/journal.pone.0082394 (2013).

49   Jaubert, J. & Bordes, J.-G.   370 (Société préhistorique française, 2008).

50   White, M. & Ashton, N. Lower Palaeolithic Core Technology and the Origins of the Levallois Method in North‐Western Europe. *Curr Anthropol* **44**, 598-609, doi:10.1086/377653 (2003).

51   Westaway, R., Bridgland, D. & White, M. The Quaternary uplift history of central southern England: evidence from the terraces of the Solent River system and nearby raised beaches. *Quaternary Sci Rev* **25**, 2212-2250, doi:http://dx.doi.org/10.1016/j.quascirev.2005.06.005 (2006).

52   Santonja, M. & Villa, P. in *Axe age : Acheulian tool-making from quarry to discard*   (eds N. Goren-Inbar & Gonen Sharon) (Equinox, 2006).

53   Grimaldi, S. Analyse technologique, chaîne opératoire et objectifs techniques. Torre in Pietra (Rome, Italie). Torre in Pietra (Rome, Italy). Technological analysis, chaîne opératoire and technical objectives. *Paléo*, 109-122 (1998).

54   Tuffreau, A. in *The Transition from the Lower to Middle Palaeolithic and the Origin of Modern Man* Vol. 151 (ed A. Ronen) 137-149 (British Archaeological Reports, International Series, 1982).

55   Gagnepain, J. & Gaillard, C. in *La grotte de la Baume Bonne (Quinson, Alpes de Haute-Provence) : synthèse chronostratigraphique et séquence culturelle d'après les fouilles récentes (1988-1997).* 73-86 (John and Erica Hedges Ltd).

56   Jarry, M., D., C., L.A., L. & V., M. *Les Bosses (La Magdelaine, Lot, France): Un gisement paléolithique moyen antérieur à l'avant-dernier Interglaciaire sur la moyenne terrasse du Lot*. (Société Préhistorique Française, 2007).

57   Van Baelen, A., Meijs, E., Van Peer, P., de Warrimont, J.-P. & De Bie, M. An early Middle Palaeolithic site at Kesselt-Op de Schans (Belgian Limburg). Preliminary result. *Notae Praehistoricae* **27**, 19-26 (2007).

58   Ryssaert, C. Lithische technologie te Mesvin IV: selectiecriteria voor geretoucheerde werktuigen en hun relatie met Levalloiseindproducten. *Anthropologica Et Praehistorica* **117**, 13-33 (2006).

59   Colonge, D. *et al.* De la transition paléolithique inférieur-moyen dans la vallée de la Garonne: l'Acheuléen supérieur de Raspide 2 (Blagnac, Haute-Garonne). *Bulletin de la Société préhistorique française* **107**, 205-225 (2010).

60   Thissen, J. *Die Paläolithischen Freilandstationen von Rheindahlen im Löss Zwischen Maas und Niederrhein*. (Rheinische Ausgrabungen 59, Verlag Philipp von Zabern, Mainz, 2006).

61   Blackwell, B. & Schwarcz, H. P. in *La Grotte Vaufrey: Paléoenvironnement, chronologie, activités humaines* (ed Jean-Philippe Rigaud) 365–380 (Mémoires de la Société Préhistorique Française, 1988).

62   Balescu, S. & Tuffreau, A. La phase ancienne du Paléolithique moyen dans la France septentrionale (stades isotopiques 8 à 6) : apports de la datation par luminescence des séquences lœssiques. *Archaeological Almanac* **16**, 5-22 (2004).

63   Wisniewski, A. & Fridrich, J. in *Middle Palaeolithic Activity and Palaeoecology*   (eds J. M. Burdukiewicz & A. Wisniewski) 217–243 (Studia Archeologiczne 41, Biblioteka Cyfrowa, Wydawnictwa Uniwersytetu Wroclawskiego, 2010).

64   Bahain, J.-J. *La méthode de datation par résonance de spin électronique (ESR) au Muséum national d'histoire naturelle. Vingt ans de recherches méthodologiques et d'applications géochronologiques*, Université Michel de Montaigne - Bordeaux III, (2007).

65   Cyrek, K., Sudoł, M., Czyżewski, Ł., Osipowicz, G. & Grelowska, M. Middle Palaeolithic cultural levels from Middle and Late Pleistocene sediments of Biśnik Cave, Poland. *Quatern Int* **326**, 20-63, doi:http://dx.doi.org/10.1016/j.quaint.2013.12.014 (2014).

66   Sun, X. *et al.* Recuperated optically stimulated luminescence dating of middle-size quartz grains from the Palaeolithic site of Bonneval (Eure-et-Loir, France). *Quat Geochronol* **5**, 342-347, doi:http://dx.doi.org/10.1016/j.quageo.2009.05.004 (2010).

67   Jaubert, J. & Servelle, C. in *L'Acheuléen dans l'Ouest de l'Europe* (ed A. Tuffreau) 77-108 (University of Sciences & Technology, Centre d'Etudes et Recherches Préhistoriques, 1996).

68   Brenet, M. *et al.* Interprétation de la variabilité technologique de deux industries du Paléolithique moyen ancien du Bergeracois : Cantalouette 1 et Combe Brune 3 (Creysse, Dordogne). *Bulletin de la Société Préhistorique Française*, 57-81 (2008).

69   Wiśniewski, A. The beginnings and diversity of Levallois methods in the early Middle Palaeolithic of Central Europe. *Quatern Int* **326**, 364-380, doi:http://dx.doi.org/10.1016/j.quaint.2013.10.027 (2014).

70   Marks, A. E. *et al.* Le gisement pléistocène moyen de Galeria Pesada (Estrémadure, Portugal) : premiers résultats. *PALEO* **14**, 77-100 (2002).

71   Adler, D. S. *et al.* Early Levallois technology and the Lower to Middle Paleolithic transition in the Southern Caucasus. *Science* **345**, 1609-1613, doi:10.1126/science.1256484 (2014).

72   Haesaerts, P. & Koulakovskaya, L. V. in *The European Middle Paleolithic* (ed L. V. Koulakovskaya) 21-38 (Shlyakh, Kiev, 2006).

73   Callow, P. & Cornford, J. M. *La Cotte de St. Brelade, 1961-1978 : excavations by C.B.M. McBurney*. (Kluwer Academic, 1986).

74   Delagnes, A. & Ropars, A. in *Paléolithique moyen en pays de Caux (Haute-Normandie). Le Pucheuil, Ettoutteville: Deux gisements de plein air en milieu loessique* (Éditions de la Maison des Sciences de l'Homme, 1996).

75   Adam, A. Les pointes pseudo-Levallois du gisement moustérien Le Rissori, à Masnuy-Saint-Jean (Hainaut, Belgique). *L'Anthropologie* **106**, 695-730, doi:http://dx.doi.org/10.1016/S0003-5521(02)01143-3 (2002).

76   Vandenberghe, J., Roebroeks, W. & van Kolfschoten, T. *Maastricht-Belvédère: Stratigraphy. Palaeoenvironment and Archaeology of the Middle and Late Pleistocene Deposits. Part II*. (Mededelingen Rijks Geologische Dienst, 1993).

77   Ameloot-van der Heijden, N., Dupuis, C., Limondin, N., Munaut, A. V. & Puissegur, J. J. The Middle Palaeolithic open air site of Salouel. *L'Anthropologie* **100**, 555-573 (1996).

78   Picin, A., Peresani, M., Falguères, C., Gruppioni, G. & Bahain, J.-J. San Bernardino Cave (Italy) and the Appearance of Levallois Technology in Europe: Results of a Radiometric and Technological Reassessment. *Plos One* **8**, e76182, doi:10.1371/journal.pone.0076182 (2013).

79   Scott, B., Ashton, N., Lewis, S., Parfitt, S. & White, M. in *The Ancient Human Occupation of Britain* (eds Nick Ashton, Simon Lewis, & Chris Stringer) 67-89 (Elsevier, 2011).

80   Locht, J.-L., Antoine, P., Hérisson, D., Gadebois, G. & Debenham, N. Une occupation de la phase ancienne du Paléolithique moyen à Therdonne (Oise). Chronostratigraphie, production de pointes Levallois et réduction des nucléus. *Gallia préhistoire*, 1-32 (2010).

81   Mallick, R. & Frank, N. A new technique for precise uranium-series dating of travertine micro-samples. *Geochim Cosmochim Ac* **66**, 4261-4272, doi:http://dx.doi.org/10.1016/S0016-7037(02)00999-7 (2002).

82   Rolland, N. The early human occupation of high latitudes, Boreal, continental and periglacial habitats: Middle Palaeolithic milestones In northern Eurasia. *Acta Universitatis Wratislaviensis* **3027**, 15-46 (2010).

83   Akhilesh, K. *et al.* Early Middle Palaeolithic culture in India around 385–172 ka reframes Out of Africa models. *Nature* **554**, 97 (2018).

84   Derevianko, A. P. *et al. Paleoenvironment and Paleolithic human occupation of Gorny Altai: subsistence and adaptation in the vicinity of Denisova Cave*. (2003).

85   Mercier, N. *et al.* Hayonim Cave: a TL-based chronology for this Levantine Mousterian sequence. *J Archaeol Sci* **34**, 1064-1077, doi:http://dx.doi.org/10.1016/j.jas.2006.09.021 (2007).

86   Hershkovitz, I. *et al.* The earliest modern humans outside Africa. *Science* **359**, 456 (2018).

87   Tensorer, J.-M. L. *et al.* Long-term site formation processes at the natural springs Nadaouiyeh and Hummal in the El Kowm Oasis, Central Syria. *Geoarchaeology* **22**, 621-640, doi:10.1002/gea.20177 (2007).

88   Petraglia, M. D. *et al.* Hominin Dispersal into the Nefud Desert and Middle Palaeolithic Settlement along the Jubbah Palaeolake, Northern Arabia. *Plos One* **7**, e49840, doi:10.1371/journal.pone.0049840 (2012).

89   Otte, M. *et al.* Long-term technical evolution and human remains in the Anatolian Palaeolithic. *J Hum Evol* **34**, 413-431, doi:http://dx.doi.org/10.1006/jhev.1997.0199 (1998).

90   Valladas, H. *et al.* Dating the Lower to Middle Paleolithic transition in the Levant: A view from Misliya Cave, Mount Carmel, Israel. *J Hum Evol* **65**, 585-593, doi:http://dx.doi.org/10.1016/j.jhevol.2013.07.005 (2013).

91   Mercier, N. & Valladas, H. Reassessment of TL age estimates of burnt flints from the Paleolithic site of Tabun Cave, Israel. *J Hum Evol* **45**, 401-409, doi:http://dx.doi.org/10.1016/j.jhevol.2003.09.004 (2003).

92   Hoffecker, J. *Desolate landscapes: Ice-Age settlement in Eastern Europe*. (2003).

93   Krivoshapkin, A. I., Kuzmin, Y. & Jull, A. J. T. Chronology of the Obi-Rakhmat Grotto (Uzbekistan): First Results on the Dating and Problems of the Paleolithic Key Site in Central Asia. *Radiocarbon* **52**, 549-554 (2010).

94   Slavinskiy, V. S. & Rybin, E. P. Levallois Convergent Unidirectional Typical Technology in Southern Siberia and the Northern Part of Central Asia: Variability, Distribution, Chronology. *Stratum Plus* **2015**, 285-307 (2015).

95   Derevianko, A. P., Postnov, P., Rybin, E. P., Kuzmin, Y. & Keates, S. G. The Pleistocene peopling of Siberia: A review of environmental and behavioral aspects. *Indo-Pacific Prehistory Association Bulletin* **25**, 57-68 (2005).

96   Rose, J. I. *et al.* The Nubian Complex of Dhofar, Oman: An African Middle Stone Age Industry in Southern Arabia. *Plos One* **6**, e28239, doi:10.1371/journal.pone.0028239 (2011).

97   Shirokov, V. N., Volkov R. B., Kosintsev, P. A. & Lapteva, E. G. Paleoliticheskaya stoyanka Bogdanovka (Yuzhnyy Ural). *Rossiyskaya arkheologiya* **1**, 111-125 (2011).

98   Svendsen, J. I. *et al.* Geo-archaeological investigations of Palaeolithic sites along the Ural Mountains – On the northern presence of humans during the last Ice Age. *Quaterny Sci Rev* **29**, 3138-3156, doi:https://doi.org/10.1016/j.quascirev.2010.06.043 (2010).

99   Pavlov, P., Roebroeks, W. & Svendsen, J. I. The Pleistocene colonization of northeastern Europe: a report on recent research. *J Hum Evol* **47**, 3-17, doi:https://doi.org/10.1016/j.jhevol.2004.05.002 (2004).

100   Petraglia, M. *et al.* Middle paleolithic assemblages from the Indian subcontinent before and after the Toba super-eruption. *Science* **317**, 114-116, doi:10.1126/science.1141564 (2007).

101   Blinkhorn, J., Achyuthan, H., Petraglia, M. & Ditchfield, P. Middle Palaeolithic occupation in the Thar Desert during the Upper Pleistocene: the signature of a modern human exit out of Africa? *Quaternary Sci Rev* **77**, 233-238, doi:DOI 10.1016/j.quascirev.2013.06.012 (2013).

102   Hidjrati, N., Kimball, L. R. & Koetje, T. A. Middle and Late Pleistocene investigations of Myshtulgaty Lagat (Weasel Cave) North Ossetia, Russia. *Antiquity* **77**, 298 (2003).

103   Chlachula, J., Drozdov, N. I. & Ovodov, N. D. Last Interglacial peopling of Siberia: the Middle Palaeolithic site Ust'-Izhul', the upper Yenisei area. *Boreas* **32**, 506-520, doi:10.1111/j.1502-3885.2003.tb01231.x (2003).

104   Vasil'ev, S. A., Kuzmin, Y. V., Orlova, L. A. & Dementiev, V. N. Radiocarbon-based chronology of the Paleolithic in Siberia and its relevance to the peopling of the New World. *Radiocarbon* **44**, 503-530 (2002).

105   Blinkhorn, J. Late Middle Palaeolithic surface sites occurring on dated sediment formations in the Thar Desert. *Quatern Int* **350**, 94-104, doi:https://doi.org/10.1016/j.quaint.2014.01.027 (2014).

106   Andrews, J. E. *et al.* Do Stable Isotope Data from Calcrete Record Late Pleistocene Monsoonal Climate Variation in the Thar Desert of India? *Quaternary Res* **50**, 240-251, doi:https://doi.org/10.1006/qres.1998.2002 (1998).

107   Wang, X. K., Wei, J., Chen, Q. J., Tang, Z. W. & Wang, C. X. A preliminary study on the excavation of the Jinsitai Cave site (in Chinese). . *Acta Anthropologica Sinica* **29**, 15-32 (2010).

108   Krause, J. *et al.* Neanderthals in central Asia and Siberia. *Nature* **449**, 902-904, doi:http://www.nature.com/nature/journal/v449/n7164/suppinfo/nature06193_S1.html (2007).

109   Liu, D. *et al.* Progress in the stratigraphy and geochronology of the Shuidonggou site, Ningxia, North China. *Chinese Sci Bull* **54**, 3880, doi:10.1007/s11434-009-0652-y (2009).

110   Li, F. *et al.* The development of Upper Palaeolithic China: new results from the Shuidonggou site. *Antiquity* **87**, 368-383 (2013).

111   Boëda, E., Hou, Y. M., Forestier, H., Sarel, J. & Wang, H. M. Levallois and non-Levallois blade production at Shuidonggou in Ningxia, North China. *Quaternary International*, doi:http://dx.doi.org/10.1016/j.quaint.2012.07.020 (2013).

112   Derevianko, A. *et al.* The stratified cave site of Tsagaan Agui in the Gobi altai (Mongolia). *Archeology, Ethnology, and Anthropology of Eurasia* **1**, 23-36 (2000).

113   Zwyns, N., Gladyshev, S., Tabarev, A. & Gunchinsuren, B. Mongolia: Palaeolithic. *Encyclopedia of Global Archaeology* **8**, 5025-5032 (2014).

114   Kreutzer, S. *et al.* Introducing an R package for luminescence dating analysis. *Ancient TL* **30**, 1-8 (2012).

115   Peng, J. & Li, B. Single-aliquot regenerative-dose (SAR) and standardised growth curve (SGC) equivalent dose determination in a batch model using the R Package 'numOSL'. *Ancient TL* **35**, 32-53 (2017).

Selected Levallois cores in 3D PDF Format

The following three pages show the CT-scanned structures of three selected Levallois cores from GYD in 3D PDF format, where the structures can be manipulated within Acrobat Reader.
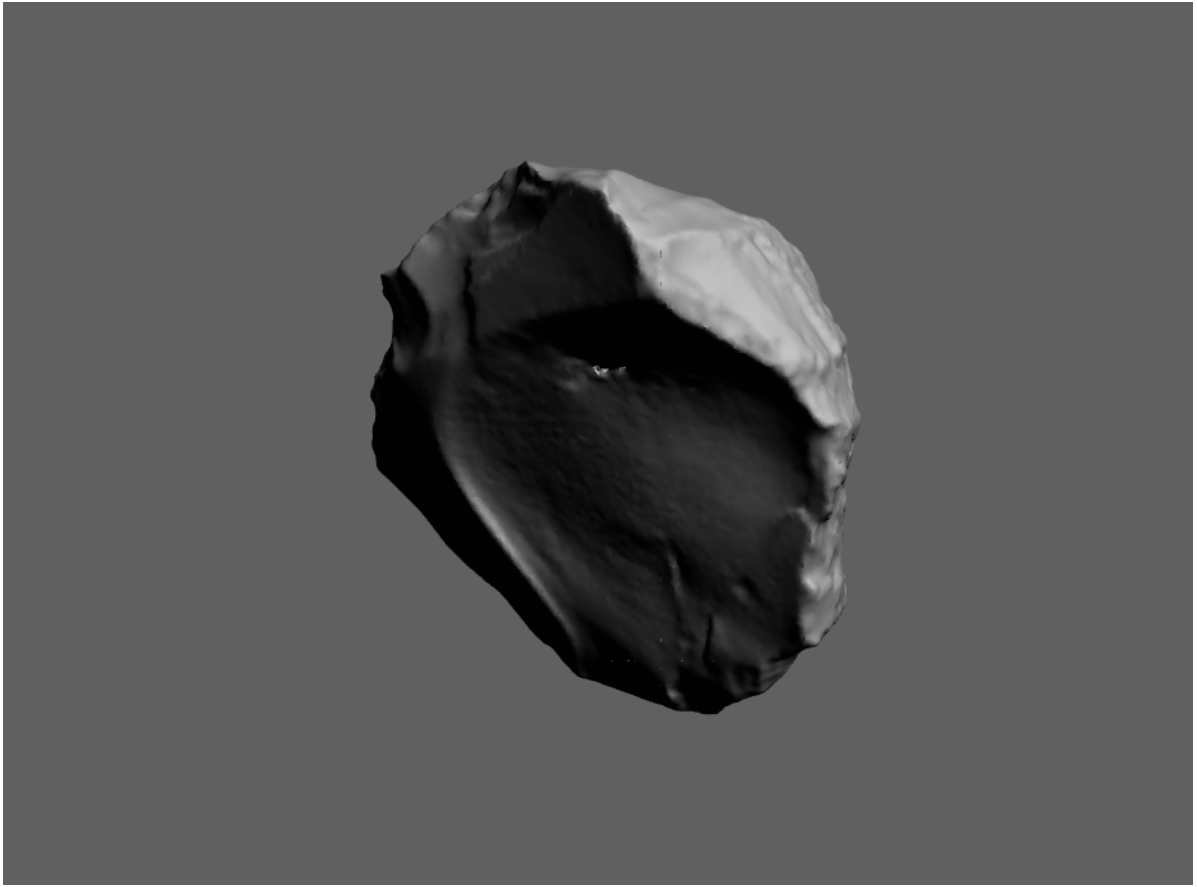
Supplementary Data 1 | The structure of a Levallois preferential core from Guanyindong Cave. The maximum dimension, length and thickness of this specimen are 83, 72 and 23 mm, respectively. This artefact is identical to that appearing in Fig. 3b and Extended Data Figure 5b.
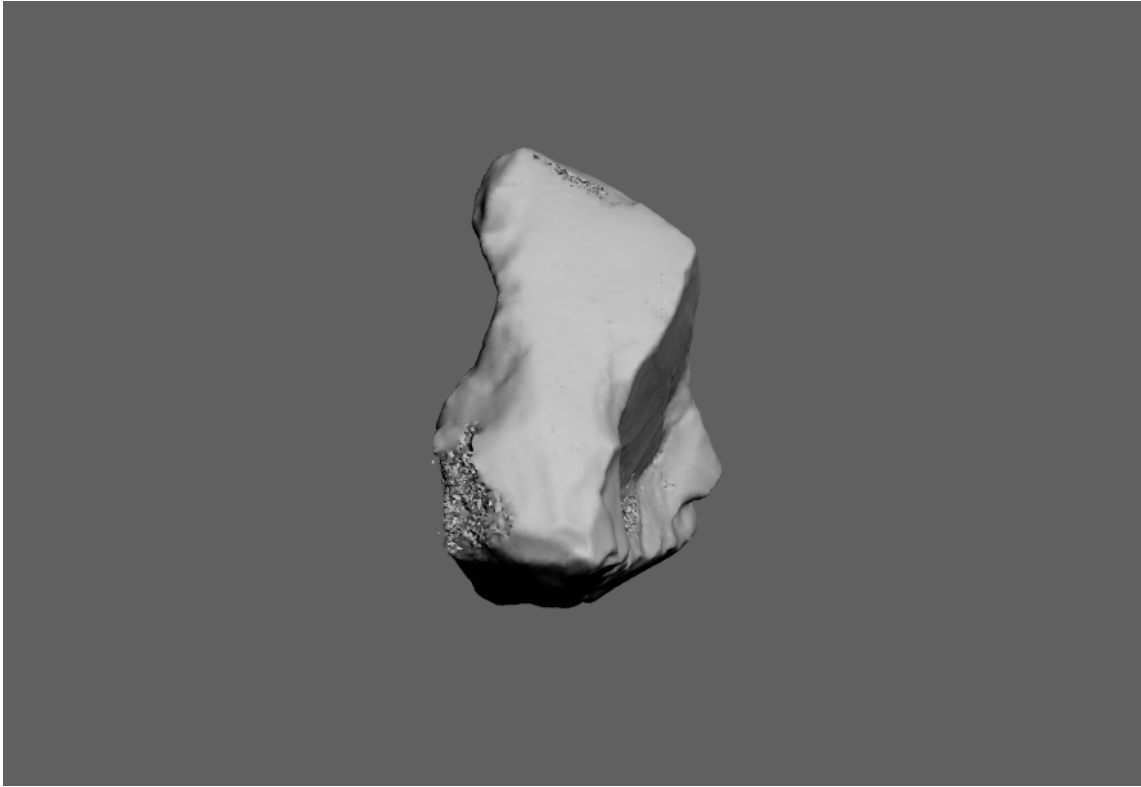
Supplementary Data 2 | The structure of a Levallois preferential core from Guanyindong Cave. The maximum dimension, length and thickness of this specimen are 86, 76 and 22 mm, respectively. This artefact is identical to that appearing in Fig. 3c and Extended Data Figure 5c.
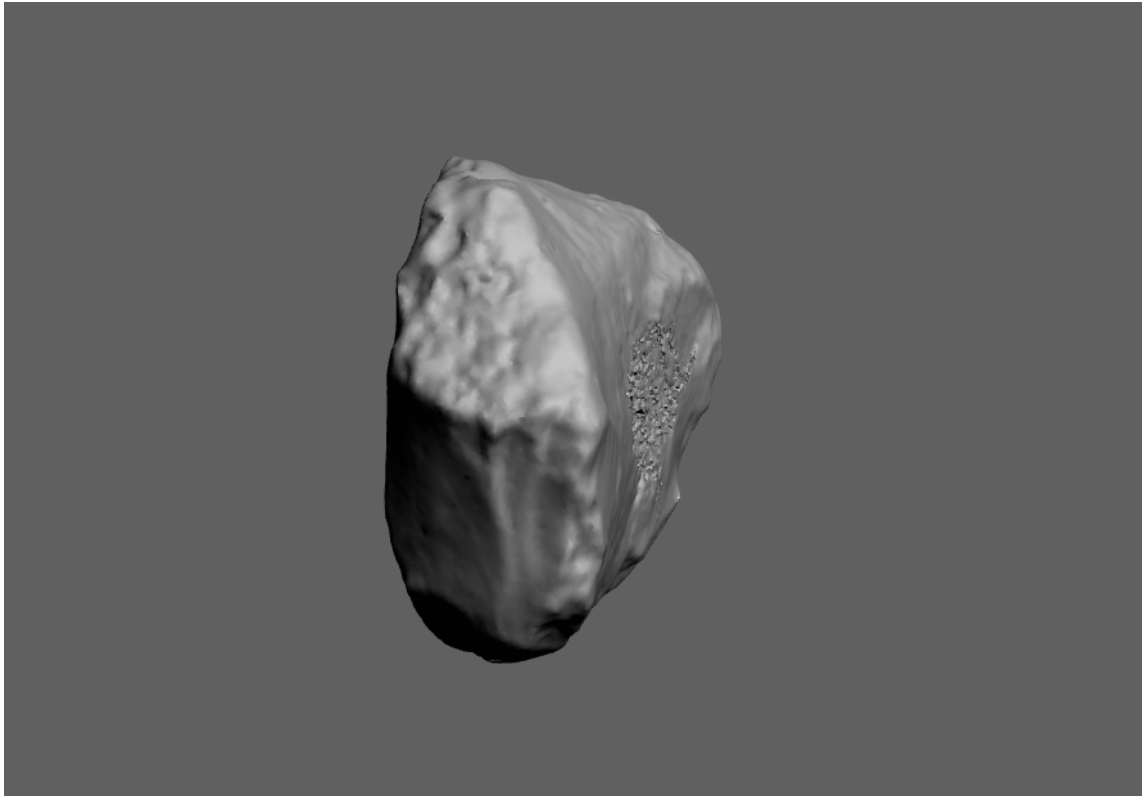
Supplementary Data 3 | The structure of a Levallois recurrent core from Guanyindong Cave. The maximum dimension, length and thickness of this specimen are 69, 56 and 21 mm, respectively. This artefact is identical to that appearing in Fig. 3a and Extended Data Figure 5a.